Check for updates

Received: 18 March 2022 | Revised: 2 September 2022 | Accepted: 10 October 2022

DOI: 10.1002/jbm.b.35185

RESEARCH ARTICLE

Sustained release of alpha-methylacyl-CoA racemase (AMACR) antibody-conjugated and free doxorubicin from silica nanoparticles for prostate cancer cell growth inhibition

Toyin Aina[1,2,3] | Ali A. Salifu[2,3] | Sonu Kizhakkepura[4] | Yiporo Danyuo[2,5] | John D. Obayemi[2,3] | Josephine C. Oparah[1,2,3] | Theresa C. Ezenwafor[1,2] | Killian C. Onwudiwe[1,2,3] | Chukwuemeka J. Ani[6] | Suchi S. Biswas[4] | Chinyerem Onyekanne[1,2,3] | Olushola S. Odusanya[7] | Jonathan Madukwe[8] | Winston O. Soboyejo[1,2,3]

[1]Department of Materials Science and Engineering, African University of Science and Technology, Abuja, Nigeria

[2]Department of Mechanical and Materials Engineering, Worcester Polytechnic Institute, Worcester, Massachusetts, USA

[3]Department of Biomedical Engineering, Worcester Polytechnic Institute, Life Sciences and Bioengineering Center, Worcester, Massachusetts, USA

[4]Chemistry and Physics of Materials Unit (CPMU), Jawaharlal Nehru Centre for Advanced Scientific Research (JNCASR) Jakkur, Bengaluru, India

[5]Department of Mechanical Engineering, Ashesi University, Accra, Ghana

[6]Department of Civil Engineering, Nile University of Nigeria, Abuja, Nigeria

[7]Biotechnology and Genetic Engineering Advanced Laboratory, Sheda Science and Technology Complex (SHESTCO), Abuja, Nigeria

[8]Department of Histopathology, National Hospital Abuja, Abuja, Nigeria

Correspondence
Winston O. Soboyejo, Worcester Polytechnic Institute, 100 Institute Road, Worcester, MA 01609, USA.
Email: wsoboyejo@wpi.edu,

Funding information
Pan African Materials Institute, Grant/Award Number: PAMI P126974

Abstract

This article presents silica nanoparticles for the sustained release of AMACR antibody-conjugated and free doxorubicin (DOX) for the inhibition of prostate cancer cell growth. Inorganic MCM-41 silica nanoparticles were synthesized, functionalized with phenylboronic acid groups (MCM-B), and capped with dextran (MCM-B-D). The nanoparticles were then characterized using Fourier-transform infrared spectroscopy, scanning electron microscopy, transmission electron microscopy, zeta potential analysis, nitrogen sorption, X-ray diffraction, and thermogravimetric analysis, before exploring their potential for drug loading and controlled drug release. This was done using a model prostate cancer drug, DOX, and a targeted prostate cancer drug, α-Methyl Acyl-CoA racemase (AMACR) antibody-conjugated DOX, which attaches specifically to AMACR proteins that are overexpressed on the surfaces of prostate cancer cells. The kinetics of sustained drug release over 30 days was then studied using zeroth order, first order, second order, Higuchi, and the Korsmeyer–Peppas models, while the thermodynamics of drug release was elucidated by determining the entropy and enthalpy changes. The flux of the released DOX was also simulated using the COMSOL Multiphysics software package. Generally, the AMACR antibody-conjugated DOX drug-loaded nanoparticles were more effective than the free DOX drug-loaded formulations in inhibiting the growth of prostate cancer cells in vitro over a 96 h period. The implications of the results are then discussed for the development of drug-eluting structures for the localized and targeted treatment of prostate cancer.

KEYWORDS
doxorubicin, drug release kinetics, prostate cancer cells, silica nanoparticles, targeted cancer drugs, α-methyl acyl-CoA racemase

 © 2022 Wiley Periodicals LLC.

15524981, 0, Downloaded from https://onlinelibrary.wiley.com/doi/10.1002/jbm.b.35185 by Egyptian National Sci. Network (Enstinet), Wiley Online Library on [08/11/2022]. See the Terms and Conditions (https://onlinelibrary.wiley.com/terms-and-conditions) on Wiley Online Library for rules of use; OA articles are governed by the applicable Creative Commons License

1 | INTRODUCTION

Prostate cancer (PC) is the most frequently diagnosed cancer second most common type of cancer in men.[1,2] It was also the fifth major cause of cancer death in 2020, with about 1.4 million new cases and 375,000 deaths worldwide. Unfortunately, the pathogenesis of PC is not well understood,[3] although age, family history of PC patients, and certain genetic mutations (e.g., BRCA1 and BRCA2) are known risk factors.[1] The highest incidence rates of PC are found in men of African descent that are also known to be highly susceptible to high risks of PC.[1–3] However, PC is most likely to develop in men during the later stages of life.[1–3] Commonly used PC treatment methods include minimally invasive ablation therapies[4–6]; radiation therapy[7]; surgery, such as radical prostatectomy[7,8]; hormone therapy[9]; cryotherapy,[10] and chemotherapy.[11]

In the case of bulk chemotherapy, significant side effects (erectile dysfunction, low libido, obesity, and bone mass loss) are often associated with the administration of relatively high concentrations of cancer drugs that need to diffuse through the blood vessels, capillaries, and pores to reach the intended cancer sites.[12] Furthermore, only a small fraction of the injected drugs reaches the intended tumor sites to induce the desired killing and shrinkage of prostate tumors. This makes the conventional bulk chemotherapy of PC difficult to achieve in practice.

There is, therefore, a need for improved methods for the localized delivery of cancer drugs to prostate tumor sites. This can be achieved by the combined use of localized drug delivery methods, and the sustained targeted delivery of cancer drugs with molecular recognition units that can interact directly with receptors that are overexpressed on the surfaces of PC cells. This need has stimulated several studies in which nanotechnology and targeted drugs have been used to develop novel methods for the detection and treatment of PC.[13–16]

Mesoporous silica nanoparticles have been widely studied as sustained release cancer drug nanocarriers to inhibit cancer cell growth.[17–21] This is due to their unique properties, such as high total specific surface area, high pore volume, large loading capacity, biocompatibility, and easy surface modification.[21]

Alpha-methylacyl-CoA racemase (AMACR) is a mitochondrial and peroxisomal enzyme involved in the beta-oxidation of dietary-branched fatty acids and C-27 bile acid intermediates.[22] Analyses of 22 studies involving 4385 participants concluded that AMACR proteins are overexpressed in PCs compared to lower expression in normal and benign prostatic tissue.[22] A recent study found that AMACR knockdown in PC cells resulted in decreased cell proliferation and increased apoptosis, suggesting that AMACR has an oncogenic role in PC.[23] Thus, AMACR proteins could be used as a biomarker for PC treatment[22,24,25] and could also be targeted by AMACR antibodies to increase the uptake of anticancer drugs, such as doxorubicin (DOX), through receptor-mediated endocytosis to specifically kill PC cells.[26]

The possibility of developing localized drug delivery structures for inhibiting the growth of PC cells will be explored in the current work using silica nanoparticles in which a model free cancer drug (DOX) and a model targeted cancer drug (AMACR antibody-conjugated DOX, DOX-A) will be released locally to target overexpressed AMACR proteins on the surfaces of PC cells. The localized and targeted release will be used to reduce the viability of PC cells under in vitro conditions. The thermodynamics and kinetics of drug release will also be discussed, along with the implications of the results for the development of sustained-release drug delivery systems for the targeted and localized treatment of PC.

In this study, we will test the hypotheses that reducing the pore sizes of the silica nanoparticles will slow down the in vitro release of the drugs (DOX and DOX-A), while capping the drug-loaded nanoparticles with dextran will further slowdown and prolong drug release to inhibit PC cell growth in vitro. Hence, mesoporous silica nanoparticles will be synthesized and functionalized with phenylboronic acid groups to reduce their pore sizes. The nanoparticles will then be loaded with the model cancer drugs (DOX and DOX-A) and capped with dextran to produce different drug-loaded nanoparticle formulations. Thus, in this work, we exploit the binding of AMACR antibodies (to which DOX is conjugated) to the AMACR proteins (antigens) overexpressed on PC cells to specifically target the cells and increase drug uptake for improved therapeutic effect.

2 | MATERIALS AND METHODS

2.1 | Materials

Tetraethyl orthosilicate (TEOS, 99%), *N*-cetyltrimethylammonium bromide (CTAB), 4-carboxyphenylboronic acid (CPBA), 1-ethyl-3-(3-dimethylaminopropyl) carbodiimide hydrochloride (EDC), *N*-hydroxysuccinimide (NHS), dextran and ethanol were purchased from Sigma-Aldrich, St. Louis, MO, United States. AMACR antibody (rabbit monoclonal, product code: BSB 5057) was procured from Bio SB, Santa Barbara, CA, United States. Sodium hydrophosphite hydrated LR, sodium hydrogen orthophosphate dehydrate, succinic anhydride, *N*,*N*-dimethylformamide (DMF), paraffin liquid heavy, and sodium hydroxide flakes were purchased from Fisher Scientific, Waltham, MA, United States. Dextran from Leuconostoc mesenteroides (MW ~50 kDa), was purchased from Sigma Aldrich. 3-Aminopropyl triethoxysilane (APTES) was obtained from Alfa Aesar, Haverhill, MA, United States, whereas DOX hydrochloride salt was supplied by LC Laboratories, Woburn, MA, United States. Toluene and hydrochloric acid were purchased from Merck, Darmstadt, Germany. All chemicals were used as received. All cell culture reagents were procured from Thermo Fisher Scientific, unless otherwise stated.

2.2 | Synthesis of MCM-41 silica nanoparticles

MCM-41 (Mobil Composition of Matter No.41) silica nanoparticles were synthesized according to the method reported by the Mobil group.[27] Briefly, 1.0 g of *N*-cetyltrimethylammonium bromide (CTAB) and 0.28 g of sodium hydroxide (NaOH) were both dissolved in 480 ml of Millipore water under continuous stirring at 600 rpm at

15524981, 0, Downloaded from https://onlinelibrary.wiley.com/doi/10.1002/jbm.b.35185 by Egyptian National Sci. Network (Enstinet), Wiley Online Library on [08/11/2022]. See the Terms and Conditions (https://onlinelibrary.wiley.com/terms-and-conditions) on Wiley Online Library for rules of use; OA articles are governed by the applicable Creative Commons License

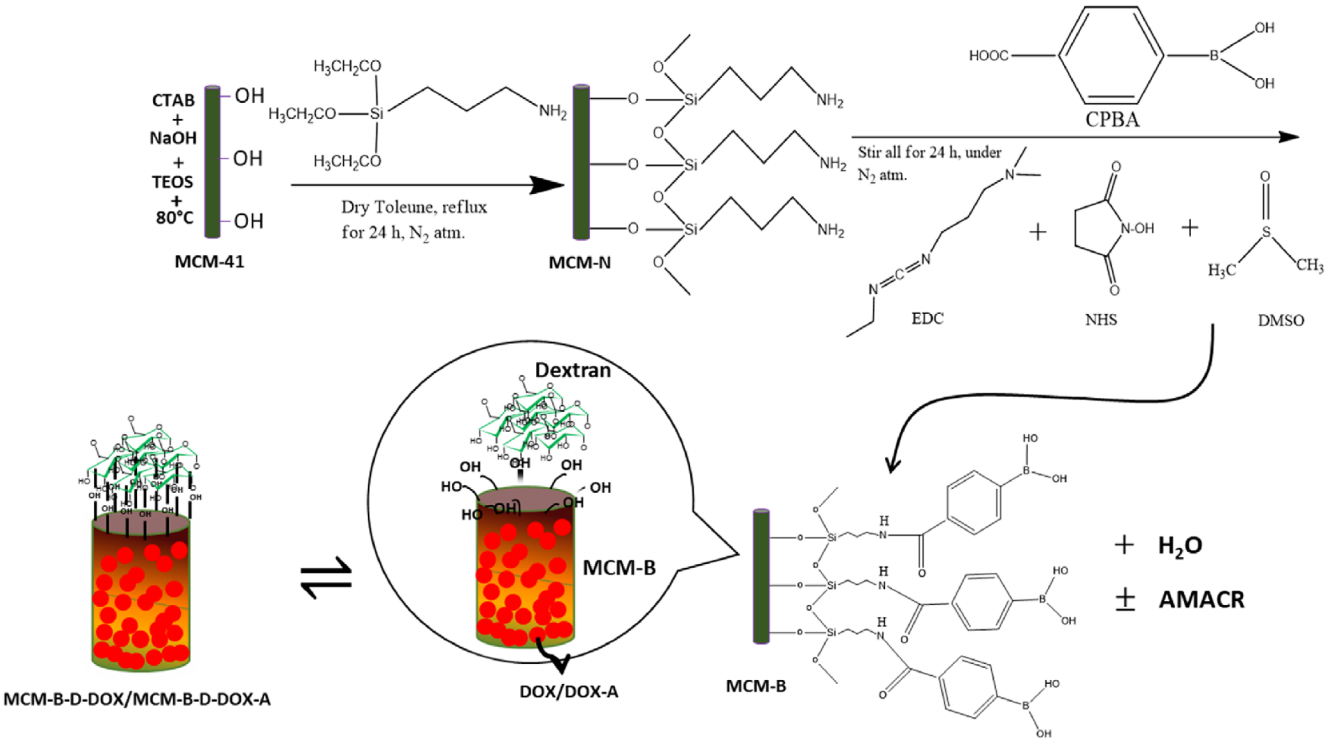


FIGURE 1 A schematic showing the steps of silanizing the silica nanoparticles (MCM-41) with amino groups (MCM-N) and followed by phenylboronic acid functionalization (MCM-B) before loading them with cancer drugs (DOX and DOX-A) and then capping the MCM-B nanoparticles with dextran. MCM, Mobil Composition of Matter

80°C in a glass bath containing paraffin and a magnetic bead to ensure homogeneity in the heating process. Next, 5 ml of tetraethyl orthosilicate (TEOS) solution was added dropwise to the CTAB/NaOH solution. After 2 h of stirring, the white solution formed was centrifuged at 12000 rpm for 5 min and the white precipitate was washed with Millipore water and ethanol and dried in oven at 60°C overnight. To knockoff the CTAB surfactant, 50 ml of ethanol was added to the white substance and the pH was adjusted to 1 with concentrated hydrochloric acid. Then, the mixture was refluxed for 6 h and washed with ethanol three times to obtain MCM-41 silica nanoparticles, which were dried in a vacuum oven at 60°C for 6 h. The dried sample was ground with a mortar and pestle to obtain a white powdered product.

2.3 | Synthesis of phenylboronic acid-functionalized MCM-41 silica nanoparticles

First, silanization of the silica nanoparticles was done by adding 1.0 ml of 3-aminopropyl triethoxysilane (APTES) to 1.0 g of the synthesized MCM-41 in a nitrogen gas environment, followed by the addition of 80 ml of anhydrous toluene and refluxing under stirring for 24 h to introduce amino groups to the nanoparticles. Afterwards, the resulting mixture was centrifuged at 12,000 rpm for 5 min and the pellet washed extensively with toluene, hexane and ethanol, and dried in a vacuum oven at 80°C for 6 h. The amount of amino groups in 1.0 mg of the silanized MCM-41 nanoparticles (referred to as MCM-N), was estimated by the ninhydrin test[28,29] to be ~30.27 wt %.

Subsequently, phenylboronic acid groups were attached to the MCM-N nanoparticles through the amino groups. First, 0.4 g of EDC and 0.2 g of NHS were dissolved in 10 ml of dry DMF in nitrogen gas inert environment, followed by the addition of 0.3 g of 4-carboxyphenylboronic acid (CPBA) under continuous stirring at 500 rpm at room temperature (RT) for 15 min. Afterwards, a dispersion of MCM-N in 40 ml of dry DMF was added to the mixture and stirred for another 24 h to tether the phenylboronic acid groups from CPBA to the amine groups attached to the MCM-N nanoparticles.

The functionalization process is illustrated in Figure 1. The resulting mixture was centrifuged at 12,000 rpm for 5 min. The pellet was washed with DMF, Millipore water and ethanol, and dried at 60°C in a vacuum oven for 6 h to obtain the phenylboronic acid -functionalized MCM-41silica nanoparticles (herein referred to as MCM-B in this article).

2.4 | Conjugation of DOX with AMACR antibody

The conjugation was done by weighing 1.0 mg of DOX and adding it to 0.5 ml of dimethyl sulfoxide (DMSO) and 88.2 μl of 2 mg/ml EDC in 0.1 M MES buffer (pH 6.0) under vigorous stirring for 40 min in the dark. 105.9 μl of 2 mg/ml NHS in 0.1 M MES buffer

15524981, 0, Downloaded from https://onlinelibrary.wiley.com/doi/10.1002/jbm.b.35185 by Egyptian National Sci. Network (Enstinet), Wiley Online Library on [08/11/2022]. See the Terms and Conditions (https://onlinelibrary.wiley.com/terms-and-conditions) on Wiley Online Library for rules of use; OA articles are governed by the applicable Creative Commons License

(pH 6.0) was then added to the reaction mixture under stirring for 20 min. AMACR antibody solution was prepared by adding 15 μl AMACR antibody to 1.2 ml of a 0.1 M $NaP0_4$/0.15 M NaCl solution with a pH of 7.5. The AMACR antibody solution was added to the reaction mixture in the dark. Then, 0.4 ml of DMSO: Water (7.5: 2.5) was added to the reaction under gradual stirring in ice for 5 h to complete the conjugation process. Excess AMACR antibody was removed from the conjugated DOX solution using a combination of 3 kDa Amicon Ultra-4 Centrifugal Filters Units, and Amicon Pro Purification System.

2.5 | Preparation of drug-loaded silica nanoparticles

The free DOX and AMACR antibody-conjugated DOX (DOX-A) drugs were loaded into the bare (MCM-41) and phenylboronic acid-functionalized (MCM-B) silica nanoparticles. This was done by adding 1 ml solutions of 2 mg/ml (in terms of their DOX content only) of DOX or DOX-A (in PBS pH 7.40) to 10 mg of the different nanoparticles, stirring for 24 h at RT, and centrifuging at 4000 rpm for 5 min. The pellet was then frozen at −80°C for 2 h and lyophilized at −105°C for 48 h using a VirTis SP Scientific BenchTop Pro Lyophilizer. The DOX-loaded MCM-41 and MCM-B nanoparticles were designated as MCM-41-DOX and MCM-B-DOX, respectively. On the other hand, their DOX-A-loaded counterparts were designated as MCM-41-DOX-A and MCM-B-DOX-A, respectively. Prior to drug loading, the concentration of DOX in DOX-A was estimated through UV–Vis measurements at 484 nm (UV-1900, Shimadzu, Tokyo, Japan).

Some of the drug-loaded MCM-B nanoparticles were capped with dextran to slow down the release of drugs from the silica nanoparticle pores after loading with drugs, as illustrated in Figure 1. The capping was done by adding 20% dextran (MW ~50 kDa) (in PBS pH 7.4) to the drug-loaded MCM-B nanoparticles and homogenizing with an Ultra Turrax T10 basic homogenizer at 30,000 rpm for 30 s. After centrifuging at 1000 rpm for 5 min, excess dextran solution was removed, and the pellet was lyophilized for 48 h. The dextran-capped MCM-B, MCM-B-DOX, and MCM-B-DOX-A nanoparticles were designated as MCM-B-D, MCM-B-D-DOX, and MCM-B-D-DOX-A, respectively. The amount of drug effectively loaded into each nanoparticle formulation was estimated through UV–Vis measurements at 484 nm (UV-1900, Shimadzu, Tokyo, Japan) to determine the concentrations of the stock drug suspension before and after drug loading. The encapsulation efficiency (EE) was then determined from Equation (1).

$$EE = \frac{C_i - C_f}{C_i} \times 100 \quad (1)$$

where C_i is the concentration of the stock drug suspension before loading and C_f is the concentration of the stock drug suspension after loading.

2.6 | Characterization of the nanoparticles

Fourier-transform infrared spectroscopy (FTIR) was used to determine the chemical bonds/functional groups that were associated with the drug-loaded and unloaded silica nanoparticles. FTIR spectra of the lyophilized samples were obtained from an FTIR spectrometer (IRSpirit, Shimadzu, Kyoto, Japan) from an average of 128 scans at a resolution of 2 cm^{-1} over a wavenumber range of 400–4000 cm^{-1}.

Thermogravimetric analysis (TGA) was used to characterize the thermal stability of the nanoparticles. Thermograms of the lyophilized samples were obtained from a TG 209 F1 Libra thermogravimetric analyzer (NETZSCH Instruments, Selb, Germany) in the temperature range of RT—900°C at a heating rate of 10°C/min in a nitrogen atmosphere with a 20 ml/min flow rate.

Nitrogen sorption analysis was carried out on the nanoparticles to determine their specific surface areas using Brunauer–Emmett–Teller (BET) theory, and their pore diameters and pore volumes using the Barrett–Joyner–Halenda (BJH) method. To this effect, 40 mg of the nanoparticles were weighed and degassed for 6 h under vacuum at 105°C. The degassed samples were then placed in sample tubes for nitrogen adsorption–desorption measurements at different relative pressures (P/P_o) using the Quantachrome Autosorb iQ gas sorption analyzer. Nitrogen adsorption–desorption isotherms were obtained at 77 K and the BET theory and BJH method were used to estimate the specific surface area and pore distribution, respectively.

X-ray diffraction (XRD) analysis was carried out on the samples using a Rigaku D/max-3A diffractometer (Rigaku Corporation, Tokyo, Japan). XRD diffractograms were obtained using a using Cu Kα radiation ($\lambda = 1.54$ Å). The samples were scanned over a range of 2θ angles between 1° and 10° at a step size of 0.05° and scan speed of 1.0 s per step.

The morphologies of the nanoparticles were examined using field emission scanning electron microscopy (FE-SEM) and transmission electron microscopy (TEM). For FE-SEM analysis, the nanoparticles were suspended in deionized water (1 mg/ml), sonicated for 30 min, and deposited on a freshly cleaved mica surface to dry. After drying, the samples were coated with gold/palladium and loaded into an FE-SEM microscope (Zeiss Gemini SEM 560, Jena, Germany) equipped with energy dispersive X-ray spectroscope (EDS) to visualize the surface morphology of the nanoparticles before and after functionalization and to determine the elemental composition of the nanoparticles. In the case of TEM analysis, the nanoparticles were dispersed in ethanol and left overnight to dry before being collected with lacey carbon films and deposited on TEM grids. Detailed morphologies of the nanoparticles were then visualized using a JEOL 4000EX high-resolution TEM microscope (JEOL, Tokyo, Japan).

Zeta potential measurements were carried out on the nanoparticles to determine their surface charge. Samples were prepared by dispersing 3 mg of the nanoparticles in 1 ml of deionized water under sonication for 30 min. Two hundred microliters of the suspensions

15524981, 0, Downloaded from https://onlinelibrary.wiley.com/doi/10.1002/jbm.b.35185 by Egyptian National Sci. Network (Enstinet), Wiley Online Library on [08/11/2022]. See the Terms and Conditions (https://onlinelibrary.wiley.com/terms-and-conditions) on Wiley Online Library for rules of use; OA articles are governed by the applicable Creative Commons License

were loaded into folded capillary zeta cells (DTS1070, Malvern Instruments, Malvern, United Kingdom) and run in a Zetasizer Nano ZS analyzer (Malvern Instruments).

2.7 | In vitro drug release

In vitro drug release studies were used to characterize the release profiles of DOX and DOX-A and to determine the kinetics and thermodynamics of sustained drug release from the silica nanoparticles. For each drug-loaded nanoparticle formulation, 5 mg of the lyophilized DOX- and DOX-A-loaded nanoparticles (MCM-41 and MCM-B) were suspended in a centrifuge tube containing 5 ml PBS buffer (at pH 6.50 and 7.40). This was used to replicate the tumor microenvironment, which is usually acidic at about pH 6.50, and the physiological condition of the body at pH 7.40.[30] The samples were prepared in triplicates. The centrifuge tubes were placed on orbital shakers within an incubator shaker (Innova 44 Incubator, Console Incubator Shaker, New Brunswick, NJ, United States) that was operated at 60 rpm at temperatures of 37, 41, and 44°C. After 3, 6, 12 and then subsequently at 24-h intervals over 30 days, 750 µl aliquots were taken out of the tubes after centrifuging them for 5 min at 4000 rpm. The tubes were replenished with 750 µl of fresh PBS, before returning them to the incubator shaker to continue the drug release studies. The absorbance values of the released drugs (DOX or DOX-A) in the aliquots were measured using a UV–Vis spectrophotometer (UV-1900, Shimadzu, Tokyo, Japan) at a wavelength of 484 nm. The concentrations of the released drugs (DOX or DOX-A) from the drug-loaded silica nanoparticle formulations were then interpolated from their respective standard curves.

2.8 | Modeling of drug release

2.8.1 | In vitro drug release kinetics

To understand the drug release kinetics, various mathematical models were used to fit the in vitro drug release data. These included: the zeroth order, first order, second order, Higuchi, and Korsmeyer–Peppas models[31,32] that are described briefly in this section.

Zeroth order release describes the release of drugs from a material medium that does not disintegrate with time. It also takes time for the medium to elute its content under equilibrium conditions.[33,34] The zeroth-order model can be expressed as:

$$C_t = C_0 + k_0 t \tag{2}$$

where C_t represents the amount of active agent released in time t, C_0 is the initial concentration of the active agent released and k_0 is the zero-order constant.[33,35]

The first order model, describes the rate at which active agents gets used up or the rate of release of the agent from a biomaterial.[32,33] First order kinetics can be represented by:

$$\frac{dC}{dt} = -k_1 C \tag{3}$$

Hence, the rate of change in concentration with respect to change in time is dependent only on concentration, where k_1 is the first order release constant.[33]

Second order kinetics model, on the other hand, can be represented by the following expression[32,36,37]:

$$\frac{1}{C_t} = \frac{1}{C_0} + k_2 t \tag{4}$$

where k_2 represents the second order rate constant, C_0 and C_t represents the initial and the final concentration of the drug at time t.

Furthermore, the Higuchi model describes the release of active agents from a solid and/or a semi-solid matrix under conditions in which the active agent is less soluble or very soluble in the matrix. Hence, the amount of drug released (e.g., concentration) is proportional to the square root of time.[33,35,38] This is given by:

$$C_t = k_H \sqrt{t} \tag{5}$$

In cases in which there is a change in concentration from C_0 to C_t and k_H, the Higuchi release constant, then the Higuchi model can be expressed as:

$$C_t = C_0 + k_H \sqrt{t} \tag{6}$$

Finally, the Korsmeyer–Peppas model describes the rate at which a polymeric material elutes its content. This model is also called the power law model, which provides a relationship between the release of the active agent (from the drug formulation) and the time taken for the release.[33,39–41]

$$\frac{M_t}{M_\infty} = kt^n \tag{7}$$

where, M_∞, M_t, t, k, and n represent the amount of drug released at equilibrium, the quantity of drug release in time t, period of drug release, release rate constant and release exponent, respectively. The above equation can also be represented in terms of concentration, where C_i is the concentration of the active agent at time t and C_∞ represents the as shown below.

$$\frac{C_t}{C_\infty} = kt^n \tag{8}$$

Hence, by taking the natural logarithm of both sides of Equation (8), we obtain Equation (9)

$$\ln\left(\frac{C_i}{C_\infty}\right) = \ln k + n \ln t \tag{9}$$

The mechanism of drug release from the various silica nanoparticle formulations was examined by fitting the drug release results to the

15524981, 0, Downloaded from https://onlinelibrary.wiley.com/doi/10.1002/jbm.b.35185 by Egyptian National Sci. Network (Enstinet), Wiley Online Library on [08/11/2022]. See the Terms and Conditions (https://onlinelibrary.wiley.com/terms-and-conditions) on Wiley Online Library for rules of use; OA articles are governed by the applicable Creative Commons License

five kinetic models presented above. The R^2 values closest to 1 were used to identify the models with the best fit.[32]

2.8.2 | In vitro drug release thermodynamics

This section presents the theoretical framework that was used to determine the thermodynamic parameters associated with controlled drug release from the silica nanoparticles. These include: the activation energy (E_a)[42]; the enthalpy change (ΔH); the sum of the internal energy change and the change in the product of the pressure and volume of a thermodynamic system[43]; the Gibbs free energy change (ΔG),[44] and the change in entropy (ΔS).[44] These were determined using methods described in detail in prior studies.[42] The Arrhenius equation (Equation 10) was used to determine the activation energy (E_a) from the slope of the plot of $\ln k_t$ versus $1/T$.

$$k_t = D_f e^{-\frac{E_a}{RT}} \tag{10}$$

$$\ln k_t = \ln D_f - \frac{E_a}{R}\frac{1}{T} \tag{11}$$

The Eyring equation (Equation 12) was used to calculate the enthalpy change (ΔH) (from the slope) and the entropy change (ΔS) (from the intercept) of the plot of $\ln k_t$ versus $1/T$

$$\ln\frac{k_t}{T} = -\frac{\Delta H}{R}\frac{1}{T} + \ln\frac{\kappa k_B}{h} + \frac{\Delta S}{R} \tag{12}$$

The change in Gibbs free energy (ΔG) was obtained from the following expression:

$$\Delta G = \Delta H - T\Delta S \tag{13}$$

where R is the universal gas constant 8.314 $Jmol^{-1}K^{-1}$, T is the absolute temperature in Kelvin, k_t is the thermodynamic equilibrium constant, E_a is the activation energy, ΔS is the change in entropy, ΔH is the change in enthalpy, κ is the transmission coefficient, k_B represents the Boltzmann constant, $1.38065 \times 10^{-23} m^2 kgs^{-2} K^{-1}$ and h represents the Planck's constant, 6.626×10^{-34} Js.

2.9 | In vitro cell viability

The in vitro viability of the PC cells with or without treatment with the DOX and DOX-A drug-loaded nanoparticles were determined using alamar blue assay to assess the cell metabolic activities, expressed as the percentage alamar blue reduction, as described previously.[32,45] A larger percentage alamar blue reduction indicates that the cells are growing faster and, as a result, are more viable. Human PC cells (PC-3 cell line, ATCC-CRL-1435) was obtained from American Type Culture Collection (ATCC), Manassas, VA, United States, and grown in a complete culture medium consisting of Kaighn's modification of Ham's medium (F-12K) supplemented with 10% fetal bovine serum (FBS) and 1% penicillin/streptomycin. The cells were maintained in a humidified incubator at 37°C and 5% CO_2. Cells were harvested at 70%–80% confluence using 0.25% trypsin–EDTA solution and subcultured in fresh T75 flasks.

At passages 5–7, $\sim 10^4$ cells/well were seeded in 24-well plates ($n = 3$) and incubated overnight at 37°C and 5% CO_2. Subsequently, the culture medium in each well was replaced with 1 ml of culture medium containing 1.0 mg/ml of the drug-loaded nanoparticles. The amount of drugs contained in 1 mg of each drug-loaded nanoparticle formulation is summarized in Table S1. The cells were also treated with 1 ml of 15 μM free DOX, 1 ml of 15 μM DOX-A and 1 ml of 1.0 mg/ml bare nanoparticles (MCM-41, MCM-B, and MCM-B-D) as controls. The nanoparticles and drugs were exposed to UV light for 3 h to sterilize them prior to adding them to the cells in the well plates.

At predetermined time intervals (0, 6, 24, 48, 72, and 96 h) after treating the cells, the culture medium was replaced with culture medium containing 10% alamar blue reagent. After incubating for 3 h at 37°C and 5% CO_2, 100 μl aliquots were transferred into black opaque 96-well plates for fluorescence intensity measurements (excitation/emission: 544/590 nm) using a 1420 Victor3 multilabel plate reader (Perkin Elmer, Waltham, MA, United States). The percentage alamar blue reduction was calculated using Equation (14).

$$\%\,\text{Alamar blue reduction} = \frac{FI_{sample} - FI_{10\%AB}}{FI_{100\%R} - FI_{10\%AB}} \times 100 \tag{14}$$

where FI_{Sample}, $FI_{10\%AB}$, and $FI_{100\%R}$ represent the fluorescence intensity of treated cells, fluorescence intensity of 10% alamar blue, and fluorescence intensity of 100% reduced alamar blue, respectively.

2.10 | Immunofluorescence staining of AMACR proteins

Immunofluorescence (IF) staining was used to study the distribution of AMACR proteins on the surfaces of the PC-3 PC cell lines. IF staining of the AMACR proteins on the PC-3 cancer cell lines were carried out as previously reported[45,46] with modifications. Briefly, 1×10^5 PC-3 cells were cultured on sterile coverslips (CELLTREAT, Pepperell, MA, United States) in 60×15 mm cell culture Petri dishes (CELLTREAT) containing 2 ml of culture medium. After incubating them in a humidified incubator at 37°C and 5% CO_2 until 70%–80% confluence, the cells were washed twice with 10% PBS solution and fixed with 4% paraformaldehyde for 15 min. The cells were then incubated with 0.1% Triton X-100 for 15 min to permeabilize them, followed by blocking with 5% normal goat serum (in PBS) for 1 h at RT (25°C). The cells were further incubated with the anti-AMACR (primary) antibody (Bio SB) for 3 h at RT and rinsed with 10% PBS solution. This was followed by incubation with the secondary antibody (Goat anti-Mouse IgG [H + L] Superclonal, Alexa Fluor 488 conjugate) for 1 h at RT and rinsing again thrice with 10% PBS solution. Finally, the nuclei were counterstained with 1 μg/ml of DAPI (in PBS) for

15524981, 0, Downloaded from https://onlinelibrary.wiley.com/doi/10.1002/jbm.b.35185 by Egyptian National Sci. Network (Enstinet), Wiley Online Library on [08/11/2022]. See the Terms and Conditions (https://onlinelibrary.wiley.com/terms-and-conditions) on Wiley Online Library for rules of use; OA articles are governed by the applicable Creative Commons License

10 min and rinsed again four times with 10% PBS solution. The coverslips were then mounted with mounting medium on glass slides and sealed with nail polish. The stained cells were then visualized with a Leica SP5 Point Scanning Confocal Microscope (Leica, Buffalo Grove, IL, United States) to obtain representative fluorescence images of the nuclei (blue color) and AMACR proteins on the surface of the PC-3 cells (green color).

2.11 | Drug release simulations

The flux of drugs from the porous nanoparticle structures was modeled using the COMSOL 5.5 Multiphysics software package. Porous structures with different pore orientations were considered in the models in which simplified homogeneity was assumed with appropriate transport across the porous surfaces.[31]

That gives:

$$\frac{\partial c}{\partial x}+\nabla.(-D\nabla c)=0 \tag{15}$$

where c represents concentration in mol/m^3 and the diffusivity D is given in m^2/s of the solute. The use of the correct initial and boundary conditions is critical in fluid exchange and diffusion studies.[47] Three boundary conditions were chosen based on the initial entry point of the fluid into the nanoparticle either from the left, right, upper part or the lower part of the geometry, with the flux exit point being the point directly opposite the entry point in a 2D geometry and the insulating boundary, while the diffusion process is ongoing.[31] In the first phase of this simulation, the boundary conditions would be set based on some defining equations.

The first boundary condition corresponds to the fluid entry boundary, and it is set as the concentration boundary. This was expressed as[31,48]:

$$c=c_0 \tag{16}$$

where c_0 is the initial concentration of the drug.

The second boundary condition represents the flux exit boundary.[31,48] This was represented as:

$$(-D\nabla_c).n=k_m(c-c_1) \tag{17}$$

Outside the porous nanoparticle, c_1 is the concentration in the bulk solution and k_m represents the mass transfer coefficient in m/s. The third boundary condition represents the insulating boundaries,[47,49] as show below.

$$(-D\nabla_c).n=0 \tag{18}$$

The initial condition is represented by an exponential function as shown below

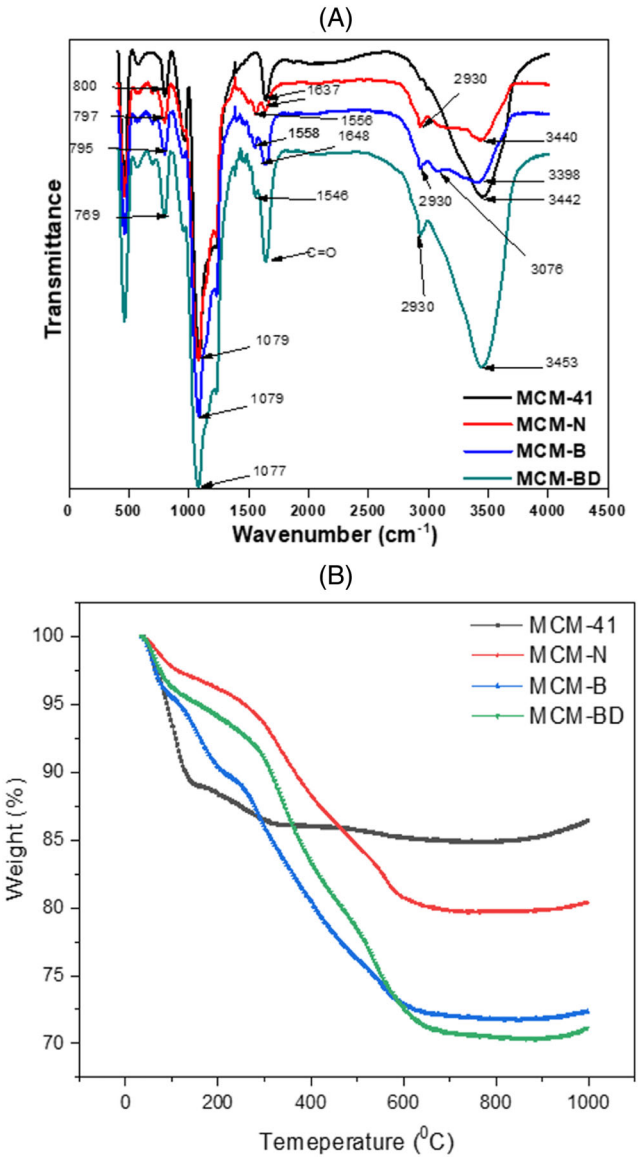


FIGURE 2 (A) Fourier-transform infrared spectroscopy (FTIR) spectra of the nanoparticles. (B) Thermogravimetric analysis (TGA) of the nanoparticles

$$c(t_0)=c_0\exp\left(-ax^2\right) \tag{19}$$

The second phase of this simulation uses a homogenous model which is in one dimension. It uses the effective properties for the modeling of fluid transport and as a result, the model equation becomes similar to the inhibited nano bubble transported through a porous medium.[47,50]

$$\varepsilon\frac{\partial c}{\partial x}+\nabla.\left(-D^{\text{eff}}\nabla c\right)=0 \tag{20}$$

where ε and D^{eff} represent the average porosity and the effective diffusion coefficient, respectively.

15524981, 0, Downloaded from https://onlinelibrary.wiley.com/doi/10.1002/jbm.b.35185 by Egyptian National Sci. Network (Enstinet), Wiley Online Library on [08/11/2022]. See the Terms and Conditions (https://onlinelibrary.wiley.com/terms-and-conditions) on Wiley Online Library for rules of use; OA articles are governed by the applicable Creative Commons License

2.12 | Statistical analysis

The results are presented as mean ± SD for three independent trials ($n = 3$), unless otherwise indicated. One-way analysis of variance (ANOVA) was used to analyze the differences in drug release from the various nanoparticle formulations, whereas two-way ANOVA was used to analyze the differences in cell viability after treatment with the nanoparticle formulations. Post hoc Tukey tests were used to identify the statistically significant groups, where p values <.05 were considered statistically significant. The analyses were carried out using the SPSS package (v28).

3 | RESULTS

3.1 | Physicochemical properties of the silica nanoparticles

To confirm the silanization and functionalization of the silica nanoparticles, the FTIR spectra of the MCM-41, MCM-N, MCM-B, and MCM-B-D are compared in Figure 2. The spectra confirmed the existence of the amino groups, the O—H group and the presence of phenylboronic acid on the silica nanoparticles.[50] The characteristic peaks for silica were observed at 798, 960, and 1079 cm^{-1} due to Si—O—Si symmetric stretching, Si—OH stretching, Si—O—Si asymmetric stretching vibrations, respectively, in all the nanoparticles. After grafting amino groups, obvious changes occurred in their spectra. The distinct bands appeared at 3364, 2930, and 1559.8 cm^{-1} owing to vibrations of the —NH_2 and N—H^+ while the Si—OH band at 960 cm^{-1} was attenuated, suggesting that most of surface silanols were reacted with aminosilane.[51] The formation of MCM-B and attachment of phenylboronic acid can also be seen (Figure 2A). A sharp band of an amine group is present at 3440 cm^{-1} in MCM-N nanoparticles, which disappears in the MCM-B nanoparticles and a broad peak appears at 3453 cm^{-1}, indicating hydroxyl groups of phenylboronic acid.[52] The C—H stretching vibrations are also present at 3042 cm^{-1}.

Amide bond formation of 4-carboxy phenylboronic acid with MCM-N and carbonyl at 1627 and 1654 cm^{-1}, respectively, confirm the formation of MCM-B.[53,54] The signals corresponding to the C═O and C—N stretches of the formed APTES linkages between the silica and the phenylboronic acid functionality in compound silica at 1654 cm^{-1} may be merged with the band of surface hydroxyl groups of silica and Si—O—Si band, respectively.[50,55]

The characteristic peaks of both dextran and MCM-B are seen in Figure 2A where the spectrum for the dextran-capped MCM-B-D is shown. In this, the distinctive vibration bands at 3453 cm^{-1} aligns with the classical signal of the polysaccharide dextran.[56,57] We also observed bands at 942 and 800 cm^{-1} representing the pyranose ring and α-D-glucose, respectively.[57] The thermal stability of the nanoparticles was tested before functionalization, and after functionalization, using TGA. From Figure 2B, the percentage weight loss due to decomposition of the nanoparticles; MCM-41, MCM-N, MCM-B, and MCM-B-D were determined to be ~15%, 20%, 27.5%, and 30%, respectively. These

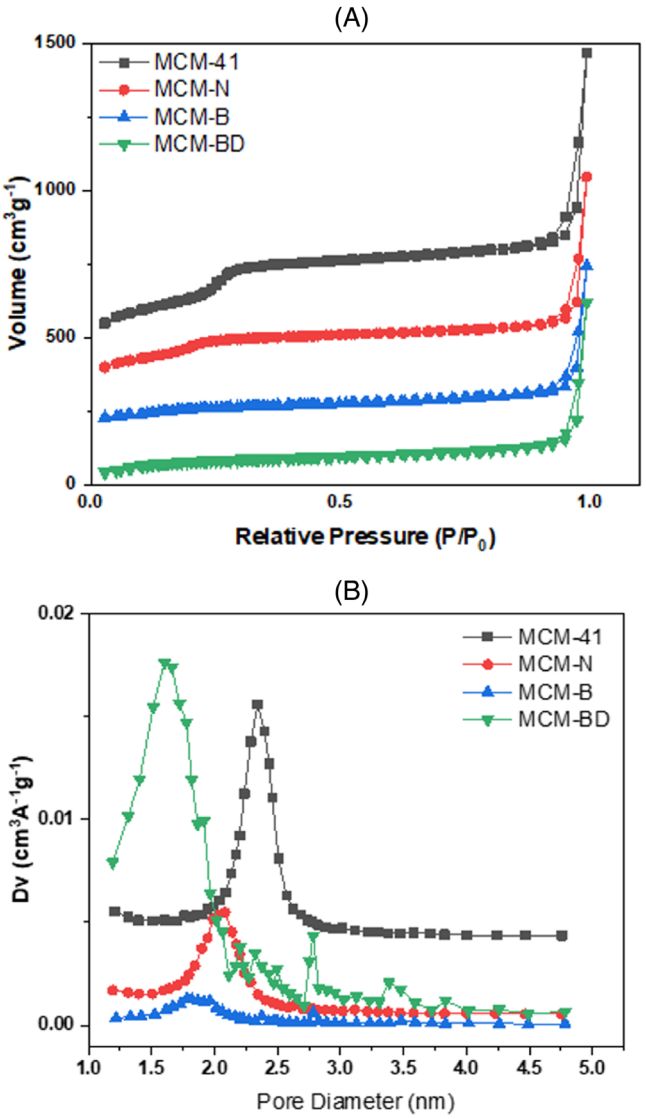


FIGURE 3 Nitrogen sorption analysis of the nanoparticles, showing the (A) nitrogen adsorption and desorption isotherms and (B) the Barret–Joyner–Halenda pore size distribution curves of the nanoparticles

imply that functionalizing the silica nanoparticles increased the rate of decomposition owing to the decomposition of the additional groups like the amine group (—NH_2) in MCM-N, phenylboronic acid group (B—O) in MCM-B, and dextran, $(C_6H_{10}O_6)n$, in MCM-B-D nanoparticles.

The results of the nitrogen sorption analysis[58] are also presented in this section and summarized in Figure 3. The synthesized MCM-41 nanoparticles had a specific surface area, pore volume and pore diameter of 1123.335 $m^2\ g^{-1}$, 1.701 $m^3\ g^{-1}$, and 2.342 nm, respectively. The BJH pore diameter was between 2 and 50 nm, indicating that the synthesized MCM-41 silica nanoparticles were mesoporous, according to the IUPAC nomenclature.[59] The silanized nanoparticle, MCM-N, had lower specific surface area, pore volume and pore diameter values of 712.773 $m^2\ g^{-1}$, 1.175 $m^3\ g^{-1}$, and 2.0842 nm, respectively, than the MCM-41 nanoparticles.

15524981, 0, Downloaded from https://onlinelibrary.wiley.com/doi/10.1002/jbm.b.35185 by Egyptian National Sci. Network (Enstinet), Wiley Online Library on [08/11/2022]. See the Terms and Conditions (https://onlinelibrary.wiley.com/terms-and-conditions) on Wiley Online Library for rules of use; OA articles are governed by the applicable Creative Commons License

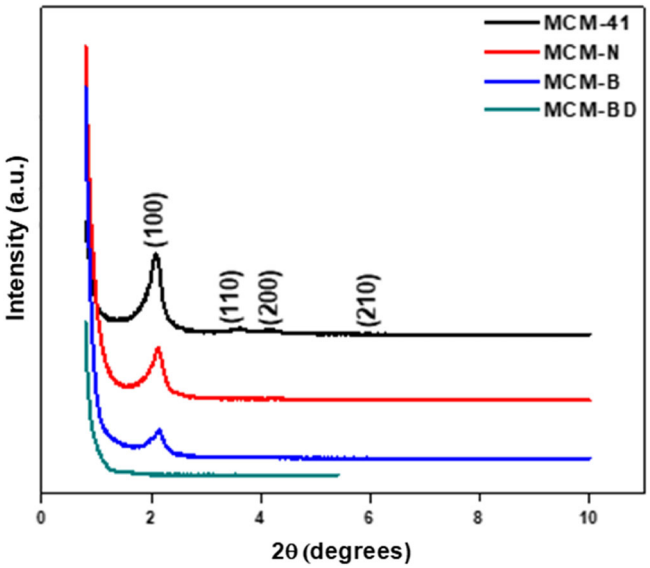


FIGURE 4 The X-ray diffraction (XRD) patterns of the nanoparticles

Further functionalization of MCM-N nanoparticle with the phenylboronic acid groups to MCM-B caused further reductions in the specific surface area, pore volume, and pore diameter to 285.568 m^2 g^{-1}, 0.869 m^3 g^{-1}, and 1.781 nm, respectively. Upon using dextran polymer to cap the pores of the MCM-B nanoparticles, slight increases were observed for the MCM-B-D than the MCM-B nanoparticles, such that the specific surface area and pore volume of MCM-B-D were greater than MCM-B by 102.261 m^2 g^{-1}, 0.123 m^3 g^{-1}, whereas the pore diameter was 0.178 nm less than that of MCM-B. The increase in the specific surface area showed that there was proper capping of the pores and the reduction in pore diameter was also due to the interaction of the matrix of the functionalized silica with the dextran that lowered the diameter.

The hexagonal symmetry of the pore ordering is shown in the XRD pattern of MCM-41 in Figure 4, which typically has four main reflection lines (d100, d110, d200, and d210) at low angles ($2\theta = 10$). MCM-41 has no atomic crystallinity since it is made up of amorphous silica.[60] From the XRD spectra in Figure 4, the peak for MCM-N, MCM-B, and MCM-B-D reduces in intensity, attributed to the functionalization effects of the amino group, phenylboronic acid group, and dextran capping, respectively. Hence, their peaks (100) occur at ~2.11°, whereas that of MCM-BD occurs at 1.57°. Furthermore, there were two other peaks that occur at 3.62°, 4.18°, and at 5.68°, which correspond to (110), (200), and (210), respectively. The peaks noticed at (110) and (200) are wide for MCM-41 and gradually disappear with further functionalization.

From the XRD spectra of all the nanoparticles, it is clear that surface functionalization of the MCM-41 with APTES and CPBA did not cause much alteration in the lattice of the silica. The broadening and gradual disappearance of the secondary peak could be due to the presence of some ligands on the pore surface of MCM-41 and or the functional groups that occupy the MCM-41 pores.[61]

Figure 5 presents the surface morphologies and elemental analysis from representative FE-SEM images and EDS spectra of the synthesized MCM-B and MCM-B-D nanoparticles. Figure 5A shows that the particles are spherical as reported in the literature.[33,62] The EDS spectrum (Figure 5C) reveals the presence of silica (19.77 wt %), confirming that the material is silica based; oxygen (52.21 wt %), suggesting the existence of the Si—O—Si bond; nitrogen (2.54 wt %) from the silanization that led to the formation of MCM-N, and boron (0.54 wt %) from the functionalization with the phenylboronic acid groups from CPBA to form the MCM-B nanoparticles. Figure 5D presents an FE-SEM image of MCM-B-D nanoparticles. The observed agglomeration of the nanoparticles shows that the gating agent, dextran, was responsible for the structure.

High resolution TEM images are presented in Figure 6. These reveal spherical nanoparticles. When these images were analyzed with Image J, the average particle sizes of the nanomaterials synthesized (MCM-B and MCM-B-D) were found to be 72.36 ± 9.06 nm and 81.97 ± 9.01 nm, respectively. The pores in the TEM images of MCM-B were more visible than that of MCM-B-D. This is attributed to the effects of dextran as a gating agent on the nanoparticle pores. Hence, the level of nanoparticle agglomeration in Figure 5E is more pronounced in MCM-B-D than in MCM-B.

The zeta potential values at pH 5.0, 6.5, and 7.4 showed that the MCM-41 nanoparticles had a negative surface charge, as shown in Table 1. This could be due to the ionization of silanol groups in aqueous solution. The surface has an acidic character, due to the possibility of proton displacement (—Si—O— + H+).[63] Upon silanizing the silica nanoparticles with amino group (MCM-N), the surface charge increased to positive values, which decreased with further functionalization with phenylboronic acid groups (MCM-B) and capping with dextran (MCM-B-D).

3.2 | Drug release from the nanoparticle formulations

Prior to the drug release studies, the amount of drug effectively loaded into the nanoparticles and the EEs were determined, and the results are summarized in Table S1. The amount of drugs loaded into the nanoparticles and the EE was generally higher for the free DOX than the AMACR antibody-DOX conjugates.

The drug release profile of DOX and DOX conjugated with AMACR antibody (DOX-A) was examined from the bare mesoporous silica nanoparticles (MCM-41), the functionalized nanoparticles with the phenylboronic acid groups (MCM-B), and the nanoparticles capped with dextran (MCM-B-D). The drug release studies were carried out using two different buffers of pH 6.5 and pH 7.4 at three different temperatures of 37°C (representing physiological temperature[64]), 41 and 44°C (representing hyperthermia temperature region[64]). The following drug-loaded formulations were used: MCM-41-DOX, MCM-41-DOX-A, MCM-B-DOX, MCM-B-DOX-A, MCM-B-D-DOX, and MCM-B-D-DOX-A. In general, the drug release profiles show that the highest DOX and DOX-A cumulative release

15524981, 0, Downloaded from https://onlinelibrary.wiley.com/doi/10.1002/jbm.b.35185 by Egyptian National Sci. Network (Enstinet), Wiley Online Library on [08/11/2022]. See the Terms and Conditions (https://onlinelibrary.wiley.com/terms-and-conditions) on Wiley Online Library for rules of use; OA articles are governed by the applicable Creative Commons License

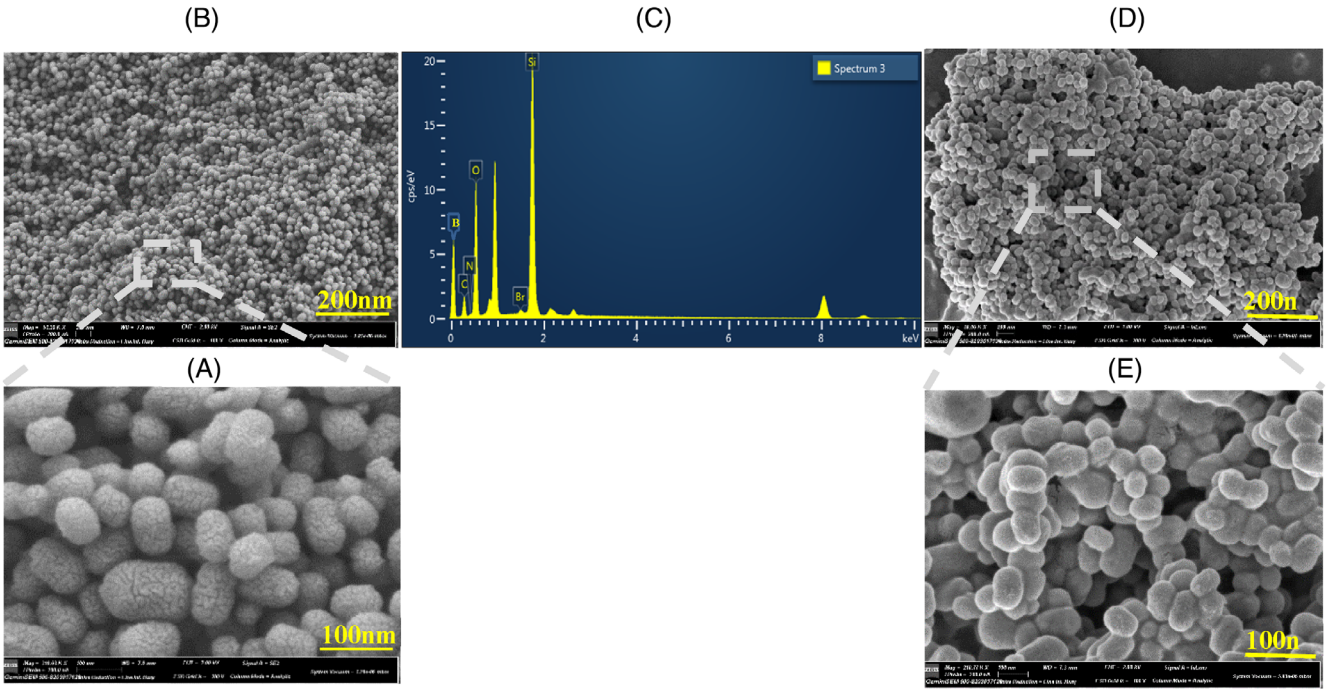


FIGURE 5 The morphology and elemental analysis of the silica nanoparticles, showing (A), (B) the field emission scanning electron microscopy (FE-SEM) micrographs of MCM-B nanoparticles. The presence of nitrogen and boron in the energy dispersive X-ray spectroscope (EDS) spectrum in (C) confirms the possible functionalization of the silica nanoparticles with amino and phenylboronic acid, respectively and (D), (E) the FE-SEM micrographs of the MCM-B-D nanoparticles. MCM, Mobil Composition of Matter

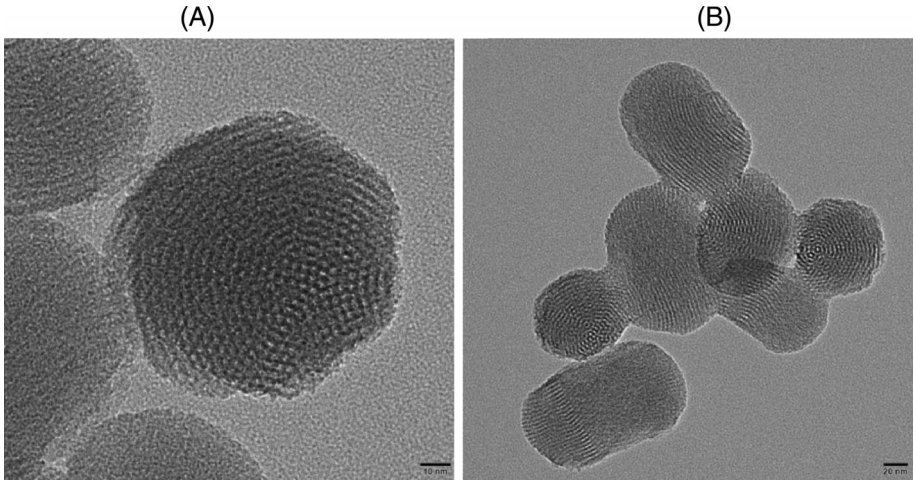


FIGURE 6 High-resolution transmission electron micrographs of (A) MCM-B nanoparticles before capping with dextran and (B) MCM-B-D nanoparticles (after capping the MCM-B nanoparticles with dextran). MCM, Mobil Composition of Matter

pH	MCM-41 (mV)	MCM-N (mV)	MCM-B (mV)	MCM-B-D (mV)
5.00	−14.73	+40.03	+34.5	+9.05
6.50	−30.77	+29.27	+11.4	+7.87
7.40	−34.33	+14.53	+12.57	+2.59

Abbreviation: MCM, Mobil Composition of Matter.

TABLE 1 A summary of the zeta potentials of the silica nanoparticles

were obtained at pH 6.5 for all the nanoparticle formulations, which is aimed at mimicking the tumor microenvironment,[36,37] as shown in Figure 7A–C,G–I.

Cumulative drug release was lower at pH 7.4, which represents the human physiological pH value.[32,36,37] This lower drug release was observed in both MCM-B and MCM-B-D but the release profile of

15524981, 0, Downloaded from https://onlinelibrary.wiley.com/doi/10.1002/jbm.b.35185 by Egyptian National Sci. Network (Enstinet), Wiley Online Library on [08/11/2022]. See the Terms and Conditions (https://onlinelibrary.wiley.com/terms-and-conditions) on Wiley Online Library for rules of use; OA articles are governed by the applicable Creative Commons License

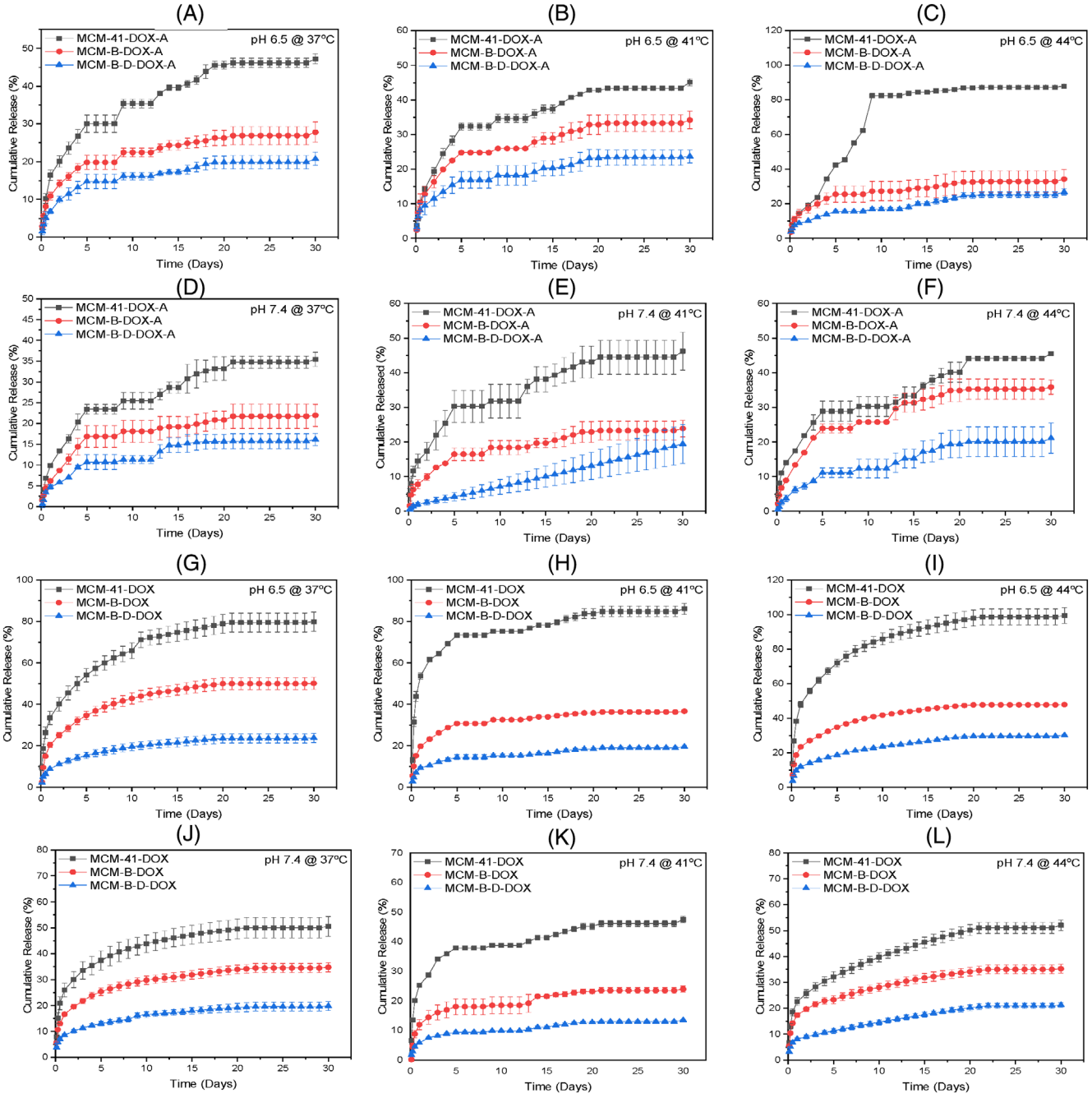


FIGURE 7 Cumulative drug release from MCM-41-DOX-A, MCM-B-DOX-A, and MCM-B-D-DOX-A of DOX-A nanoparticles in a buffer of pH 6.5 at (A) 37°C, (B) 41°C, (C) 44°C, and in a buffer of pH 7.4 at (D) 37°C, (E) 41°C, (F) 44°C. Furthermore, the cumulative drug release from MCM-41-DOX, MCM-B-DOX, and MCM-B-D-DOX of DOX nanoparticles in a buffer of pH 6.5 at (G) 37°C, (H) 41°C, (I) 44°C, in a buffer at pH 7.4 at (J) 37°C, (K) 41°C, (L) 44°C. MCM, Mobil Composition of Matter

the latter was lower than that of the former, as shown in Figure 7A–F for the conjugated drug (DOX-A) and Figure 7G–L for the free drug (DOX), meaning that capping the nanoparticle with a polymer can slow down the release of DOX and DOX-A in silica-based nanoparticle drug formulations over a period of time. In this study, the release was sustained for a period of 30 days. Hence, the reduction in the cumulative release is attributed to the capping of the pores by dextran, as well as the increase in the acidity of the buffer. The release profile also tends to increase beyond 50%, with MCM-41 having the highest cumulative release and MCM-B-D having the least cumulative release, as shown in Figure 7 for the conjugated drug and the free drug-loaded nanoparticles. The release studies also showed that the highest cumulative drug release was obtained at 44°C, while at 37°C the lowest drug release was obtained, as shown in Figure 7A,D,G,J.

Five kinetic models (Zeroth order model, First order model, Second order model, Higuchi model, and Korsmeyer–Peppas model) were

15524981, 0, Downloaded from https://onlinelibrary.wiley.com/doi/10.1002/jbm.b.35185 by Egyptian National Sci. Network (Enstinet), Wiley Online Library on [08/11/2022]. See the Terms and Conditions (https://onlinelibrary.wiley.com/terms-and-conditions) on Wiley Online Library for rules of use; OA articles are governed by the applicable Creative Commons License

TABLE 2 Thermodynamic parameters of MCM-41, MCM-B, and MCM-B-D nanoparticles loaded with doxorubicin (DOX) and doxorubicin conjugated with AMACR antibody (DOX-A)

Formulations	Temperature (°C/K)	E_a (kJ mol^{-1})	ΔH (kJ mol^{-1})	ΔS (kJ mol^{-1} K^{-1})	ΔG (kJ mol^{-1})
MCM-41-DOX	37/310.15				133.58
	41/314.15	10.973	13.58	−0.3869	135.13
	44/317.15				136.29
MCM-B-DOX	37/310.15				126.76
	41/314.15	7.107	9.714	−0.3774	128.27
	44/317.15				129.40
MCM-B-D-DOX	37/310.15				140.55
	41/314.15	37.534	14.548	−0.4063	142.18
	44/317.15				143.40
MCM-41-DOX-A	37/310.15				113.13
	41/314.15	6.488	3.882	−0.352	114.53
	44/317.15				115.59
MCM-B-DOX-A	37/310.15				114.10
	41/314.15	21.403	18.79	−0.307	115.33
	44/317.15				116.25
MCM-B-D-DOX-A	37/310.15				114.08
	41/314.15	20.086	17.479	−0.311	115.32
	44/317.15				116.26

Abbreviation: MCM, Mobil Composition of Matter.

used to characterize in vitro drug release kinetics from the silica-based nanoparticle drug formulations.[65] Table S1 shows the correlation coefficients R^2 obtained for the release kinetics. The release kinetics for the various silica-based nanoparticle formulations with the highest R^2 correlation coefficients value fits the Korsmeyer–Peppas model, as shown in Table S2. The release exponents for the free drug-loaded formulations MCM-41-DOX and MCM-B-DOX range from $0.43 \leq n \leq 0.71$ which corresponds to anomalous transport,[39,66] while MCM-B-D-DOX exhibited anomalous transport at 37°C, quasi-Fickian diffusion at 41°C and a Fickian diffusion at 44°C. The conjugated drug-loaded formulations, on the other hand, predominantly exhibited quasi-Fickian diffusion.[66] This conclusion was drawn based on the standard created from drug release from a spherical drug formulation by Peppas and Sahlin.[66]

The thermodynamic parameters computed from in vitro drug release data are presented in Table 2. The change in Gibbs free energy ΔG value for MCM-41, MCM-B and MCM-B-D were all positive, indicating the nonspontaneous nature of the release of drugs from the nanoparticles. This nonspontaneous process could be ascribed to interactions of the loaded drugs with the nanoparticles MCM-41, MCM-B, and MCM-B-D, which most likely aided the sustained drug release over a period of 30 days.[32] The change in the enthalpy (ΔE_a) was found to have a positive value, indicating that drug release from the aforementioned nanoparticles was by an endothermic process.[46,67] There was also a reduction in system disorder when the drug dispersed in the medium tried to attain equilibrium, the very small negative readings of the entropy change (ΔS) for all the nanoparticle formulations clearly confirmed this. The activation energy (E_a) indicates the amount of energy needed to transfer the drug molecule from the silica-based drug formulation to the media (e.g., PBS or PC-3 cells). Hence, the positive value of the activation energy indicated that the in vitro drug release was mostly due to processes relating to anomalous transport mechanisms, super case II or quasi Fickian diffusion.

3.3 | Simulation of drug release

In this work, drug elution was simulated from five porous geometries (Figure S1). The following assumptions were made in the simulations:

i. First, it was assumed that the porous structure was 2D and formed from the agglomeration of millions of nanoparticles with the mesopore interconnected to form the bulk material.
ii. Second, the fluid was assumed to be flowing from one boundary of the 2D rectangular geometry to the other end while keeping the third and fourth boundaries as insulating boundaries. After designing the 2D geometry, the fluid in each case was assumed to be flowing from the concentration boundary to the flux boundary, which are always perpendicular to each other. The two other boundaries were assumed to be insulating.
iii. The five geometries in Figure S1 were used in time-dependent studies that were used to simulate drug elution over periods between 10 and 30 days. The five geometries were designed with different orientations to control the directions of flow.

15524981, 0, Downloaded from https://onlinelibrary.wiley.com/doi/10.1002/jbm.b.35185 by Egyptian National Sci. Network (Enstinet), Wiley Online Library on [08/11/2022]. See the Terms and Conditions (https://onlinelibrary.wiley.com/terms-and-conditions) on Wiley Online Library for rules of use; OA articles are governed by the applicable Creative Commons License

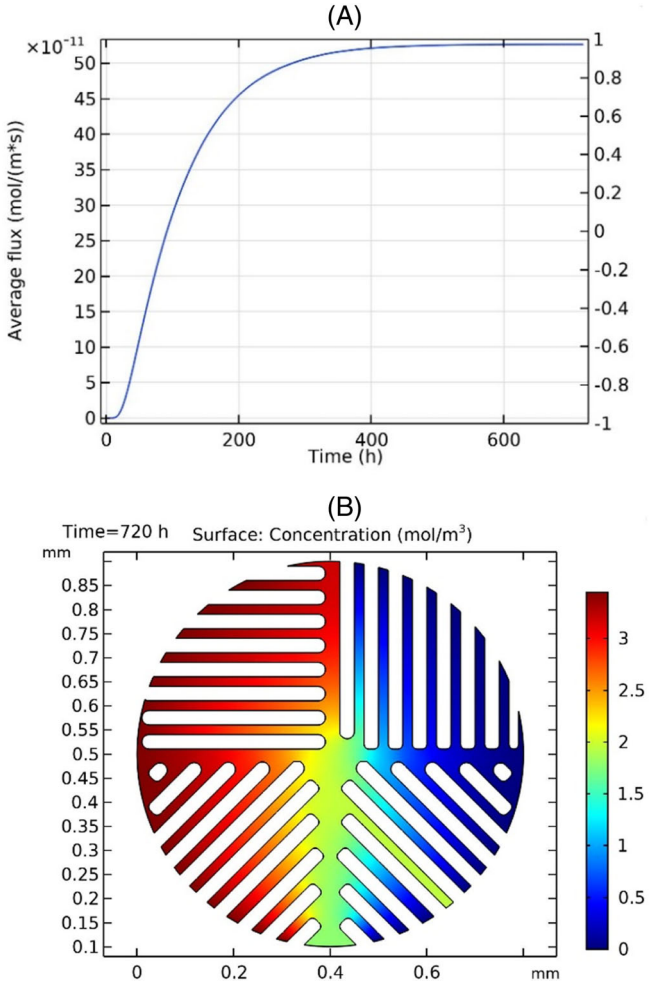


FIGURE 8 (A) Average flux of the drugs through the multiple pores of the nanomaterial over a 30-day period and (B) time-dependent transport of diluted species from the concentration boundary to the left down to the flux boundary to the right

For each of the geometries in Figure S1, the simulation was run for a period of 720 h (30 days). Steady state conditions were reached at different times, for the different geometries in Figure S1. In the case of Figure S1A, steady state was reached between $t = 0$ h to $t = 240$ h.

The average flux from the 2D model can be obtained by solving the average flux equation below

$$N_{\text{average}} = \frac{1}{L_0}\int_0^{L_0} k_m(c - c_1)dS \tag{21}$$

where L_0 corresponds to the length over the flux boundary. At steady state, the average flux can be obtained from Equation (21). The effective diffusion was also obtained from.

$$D^{\text{eff}}\frac{(c_0 - c_{\text{out}})}{L_1} = N_{\text{average}} \tag{22}$$

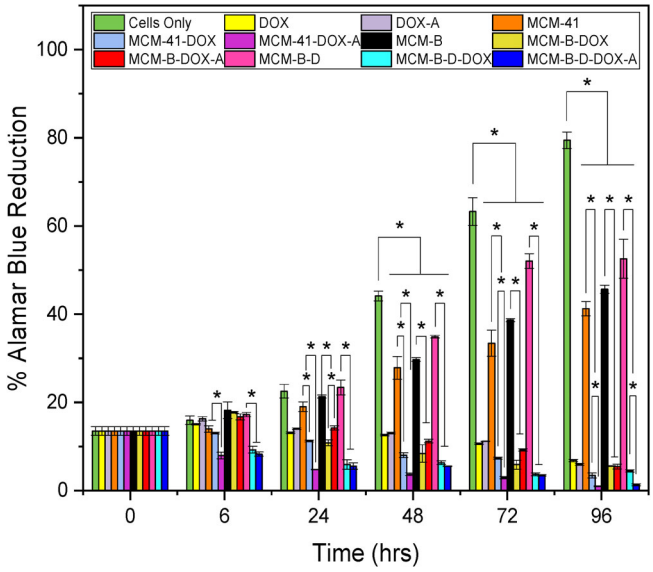


FIGURE 9 The effects of the different drug-loaded nanoparticle formulations on the viability of prostate cancer cells treated with them, as measured by the percentage alamar blue reduction. The error bars represent the SDs for $n = 3$ independent trials. *$p < .05$

where L_1 is the length of the 2D geometries that were created along the x-axis, and it is the average concentration at the flux border. Integrating according to the expression below yields the average concentration:

$$c_{\text{out}} = \frac{1}{L_0}\int_0^{L_0} c dy \tag{23}$$

The relationship between the free diffusion coefficient and the effective diffusion coefficient is given by:

$$D^{\text{eff}} = D\frac{\varepsilon}{\tau} \tag{24}$$

where τ represents the tortuosity in length per unit length of diffusion through a porous medium, and the porosity of the particle is represented as ε. At the end of the simulation, a relationship was established between the 1D homogenized model and the drug release profile as shown in Figure 8.

3.4 | Viability of PC cells

In order to use the AMACR antibody-conjugated drug-loaded nanoparticles to specifically target the PC cells, it was necessary to demonstrate the expression of AMACR proteins on these cells. The confocal fluorescence images in Figure S2 show that AMACR proteins (green color) are expressed on the surfaces of the PC-3 PC cell line. Upon

15524981, 0, Downloaded from https://onlinelibrary.wiley.com/doi/10.1002/jbm.b.35185 by Egyptian National Sci. Network (Enstinet), Wiley Online Library on [08/11/2022]. See the Terms and Conditions (https://onlinelibrary.wiley.com/terms-and-conditions) on Wiley Online Library for rules of use; OA articles are governed by the applicable Creative Commons License

binding anti-AMACR primary antibody to the AMACR proteins on fixed PC-3 cells and labeling them with Alexa Fluor 488-conjugated secondary antibody, the green fluorescence of the Alexa Fluor 488 dye was seen at areas with AMACR proteins under a confocal fluorescence microscope.

Cell metabolic activity, as measured by the percentage alamar blue reduction, was used as an indirect measure of cell viability. Thus, a higher percentage alamar blue reduction value corresponded to greater cell viability. The percentage alamar blue reduction by the PC-3 PC cells treated with the unloaded drugs (DOX and DOX-A) and the different bare and drug (DOX and DOX-A) loaded nanoparticles was quantified at times 0, 6, 24, 48, 72, and 96 h after treatment, and the results are shown in Figure 9. Treating the PC-3 cells with the various formulations significantly reduced ($p < .05$) the PC-3 cell viability after 96 h. Also, cells exposed to the drug-free nanoparticles generally exhibited higher cell viabilities than those treated with the drug-loaded nanoparticles, suggesting that the drugs released from the latter exerted anti-proliferative effects on the PC-3 cancer cells.

After 96 h of treatment, the DOX-loaded nanoparticles (MCM-41-DOX) reduced ($p < .05$) the PC-3 cell viability than the bare nanoparticles (MCM-41). When exposed to the DOX-A-loaded nanoparticles (MCM-41-DOX-A) the PC-3 cell viability further declined ($p < .05$). The PC-3 viability under treatment with MCM-B-D nanoparticles displayed a similar trend as the MCM-41 nanoparticles above (i.e., MCM-B-D-DOX-A < MCM-B-D-DOX < MCM-B-D). Both the DOX-A-loaded MCM-41 (MCM-41-DOX-A) and MCM-B-D (MCM-B-D-DOX-A) nanoparticles gave rise to the lowest PC-3 cell viability after 96 h, and there was no significant difference in cell viability between these two groups at 96 h ($p > .05$). On the other hand, there was no significant difference between the cell viabilities associated with the DOX and DOX-A-loaded MCM-B nanoparticles (MCM-B-DOX vs. MCM-B-DOX-A) ($p > .05$), although these were significantly lower than ($p < .05$) the bare MCM-B nanoparticles.

Finally, after 96 h of treatment, no significant differences ($p > .05$) were observed between the viabilities of PC-3 cells exposed to the unloaded drugs directly added (DOX and DOX-A), on one hand, and the MCM-41-DOX, MCM-B-DOX, MCM-B-DOX-A, and MCM-B-D-DOX drug-loaded nanoparticles, on the other. However, the viability of the cells treated with MCM-DOX-A and MCM-B-D-DOX-A drug-loaded nanoparticles were lower than ($p < .05$) those treated with DOX and DOX-A alone.

4 | DISCUSSION

The main goal of this study was to design a silica nanoparticle-based drug delivery system for the sustained release of model targeted and free cancer drugs (AMACR antibody-conjugated and free DOX, respectively) to inhibit the growth of PC cells. We hypothesized that functionalizing mesoporous silica nanoparticles with phenylboronic acid groups to reduce their pore sizes would slow down the release of targeted or free DOX drugs loaded into their pores. We also hypothesized that capping the drug-loaded phenylboronic acid-functionalized silica nanoparticles with a polymer (dextran) would slow down the targeted or free DOX drug release even further.

To test these hypotheses, MCM-41 silica nanoparticles were synthesized. These were then functionalized with phenylboronic acid groups (MCM-B) that were tethered to amino groups previously grafted onto the MCM-41 nanoparticles. FTIR analysis (Figure 2) confirmed the formation of silica through the peaks for Si-O-Si symmetric stretching, Si—OH stretching, and Si—O—Si asymmetric vibrations observed at 798, 960, and 1079 cm^{-1}, respectively. After grafting amino groups onto the MCM-41 silica nanoparticles to form MCM-N, distinct FTIR bands for amino groups were observed, which disappeared when the amino groups were tethered to phenylboronic acid groups to form MCM-B. An amide bond was expected to be formed between the amino groups of MCM-N and the display of peaks for C═O and C—N stretching at ~1654 and ~1627 cm^{-1} confirmed the formation of MCM-B nanoparticles.[51,53]

The FE-SEM micrographs (Figure 5) showed that the silica nanoparticles were spherical in shape. However, the MCM-B-D nanoparticles were agglomerated due to the gelling effects of the dextran used to cap the nanoparticles. The spherical shapes were more evident when the nanoparticles were visualized at higher magnifications under high resolution TEM (Figure 6). The TEM micrograph also revealed the pores on the silica nanoparticles. Using Image J to analyze the TEM images, the average diameter of the MCM-B nanoparticles was measured to be 72.36 ± 9.06 nm, which increased to 81.97 ± 9.01 nm upon capping with dextran.

Nitrogen sorption analysis indicated that the MCM-41 silica nanoparticles were mesoporous, but the pore volume and the pore diameter decreased, as expected, upon functionalizing the MCM-41 nanoparticles with phenylboronic acid groups to form MCM-B nanoparticles. Therefore, DOX was loaded into the pores of the MCM-41 and MCM-B nanoparticles as a model PC drug.

AMACR proteins have been reported to be overexpressed on the surfaces of PC cells.[68] To this end, we stained for AMACR proteins on the PC-3 PC cell lines using immunofluorescence, and the confocal fluorescence images captured (Figure S2) indicated that AMACR proteins were expressed on the PC cells. Therefore, we conjugated AMACR antibodies to DOX (DOX-A) that could bind to these expressed AMACR proteins to specifically target the PC cells for killing by the attached DOX drug. On this basis, the DOX-A drug was also loaded into the pores of the silica-based nanoparticles (MCM-41 and MCM-B).

There is a need to slow down the release of DOX-based drugs in smaller doses due to their high toxicity so as to reduce their side effects on healthy tissues. Thus, we capped the drug-loaded MCM-B nanoparticles with dextran to form MCM-B-D drug-loaded nanoparticles. FTIR analysis (Figure 2A) confirmed the existence of dextran characteristic peaks at ~3453, ~942, and ~800 cm^{-1},[49,50] in addition to the silica and phenylboronic acid peaks observed earlier, suggesting that dextran was successfully capped around the MCM-B nanoparticles.

TGA analysis (Figure 2B) showed that there were successive weight losses after functionalizing the MCM-41 nanoparticles with

15524981, 0, Downloaded from https://onlinelibrary.wiley.com/doi/10.1002/jbm.b.35185 by Egyptian National Sci. Network (Enstinet), Wiley Online Library on [08/11/2022]. See the Terms and Conditions (https://onlinelibrary.wiley.com/terms-and-conditions) on Wiley Online Library for rules of use; OA articles are governed by the applicable Creative Commons License

phenylboronic acid groups and capping them with dextran. These excess weight losses were attributed to the decomposition of the additional groups (amino and phenylboronic acid groups and dextran), thus, indicating the successful grafting of phenylboronic acid groups and dextran to the silica nanoparticles. These observations were corroborated by the XRD patterns in Figure 4, which display characteristic peaks for MCM-41 silica nanoparticles that gradually disappeared with functionalization (MCM-B) and dextran capping (MCM-B-D).

We also determined the surface charges of the nanoparticles through zeta potential measurements at pH values corresponding to physiological conditions (pH 7.4) and the tumor microenvironment (pH 5.0 and 6.5). The negative surface charges of the MCM-41 nanoparticles were attributed to their negatively charged silanol groups.[57] When silanized to introduce amino groups to its structure, the MCM-N nanoparticles exhibited positive surface charges consistent with the protonation of the —NH2 (amino) group, which confirmed the grafting of the amino groups to the MCM-41 nanoparticles. Tethering the phenylboronic acid groups to the amino groups decreased the positive surface charges of the MCM-B nanoparticles due to the negatively charged carboxyl groups of the phenylboronic acid, providing evidence for the successful grafting of phenylboronic acid groups to the MCM-41 nanoparticles. Further evidence was obtained from the EDS elemental analysis of the MCM-B nanoparticles (Figure 5C), which revealed the presence of silica and oxygen (from the MCM-41 nanoparticles), nitrogen (from the grafted amino groups), and boron (from the phenylboronic acid groups tethered to the MCM-41 nanoparticles).

After successfully synthesizing and characterizing the silica-based nanoparticles and loading them with the model drugs (DOX and DOX-A), the next part of this study was to test the hypothesis that reducing the pore sizes of the mesoporous silica nanoparticles (MCM-41) through functionalization with phenylboronic acid groups (MCM-B) and capping the pores with dextran (MCM-B-D) would slow down and prolong the release of the model drugs (DOX and DOX-A) from the nanoparticles. The drug release studies were carried out in phosphate-buffered saline (PBS) at pH 7.4 and pH 6.5, corresponding to the physiological and slightly acidic tumor microenvironments, respectively, and at physiological (37°C) and hyperthermic temperatures (41 and 44°C).

It is evident from the drug release profiles (Figure 7) that there was a higher cumulative release of drugs (DOX and DOX-A) from the nanoparticles at pH 6.5 than at pH 7.4. This was probably the result of the protonation of DOX and DOX-A in the acidic environment (pH 6.5) that weakened the electrostatic interactions between the drugs (DOX and DOX-A) and the silica nanoparticles,[19] thus, releasing more drugs into the buffer. It is, therefore, expected that these drug-loaded silica nanoparticles would elute the drugs (DOX and DOX-A) to the prostate tumor region when they are administered since the tumor microenvironment is acidic.[61–63]

As shown in Figure 7, the cumulative drug release was generally higher for the drug-loaded MCM-41 nanoparticles. However, functionalizing the MCM-41 with the phenylboronic acid groups (MCM-B) reduced the BJH pore volume and pore diameter by ~49% and ~24%, respectively. The lower cumulative release from the MCM-B nanoparticles is, therefore, attributed to the significant reduction in the pore sizes that slowed down the release of the loaded drugs (DOX and DOX-A). Drug release was further slowed down when the drug-loaded MCM-B nanoparticles were capped with dextran (MCM-B-D). This was consistent with the reduction in the BJH pore size distribution observed in Figure 3B for the MCM-B-D nanoparticles. The slowdown in drug release was also attributed to the nonspontaneous nature of the release as determined from the thermodynamic parameters.

It must be pointed out that the weight of the DOX-A molecules was expected to increase by ~54 kDa (the molecular weight of the AMACR antibody), which will also increase the molecule size. As a result, the amount of DOX-A that can be loaded into the nanoparticle pores will decrease compared to the free DOX that has a smaller molecular weight and size. In addition, the larger molecular weight and size will slow down the release of DOX-A drugs from the pores. This contributed to the lower amounts of DOX-A loaded into the nanoparticles (Table S1) and the lower cumulative drug release profiles observed for the DOX-A formulations (Figure 7) than the free DOX formulations.

In this study, it was observed that the percentage cumulative drug released (Figure 7A–L) occurred in two phases for the DOX-loaded nanoparticles (Figure 7A–F), with the first phase being moderate all through to day 20, while the remaining 10 days showed that the drug release profile was linear. In the case of DOX-A-loaded nanoparticles (Figure 7G–L), it exhibited three phases. The first phase exhibited a very fast cumulative drug release within the first 5 days study, for the next 15 days the release was considerably reduced. Hence the moderate slope of the curve. The last 10 days looks considerably consistent up till day 30 with the slope being almost linear. Hence the first phase drug release is as a result of drug burst release,[69] while the second and the last phases of DOX-A release could be as a result of steady state drug release.[70]

As a result of the initial exposure of the nanoparticles to the phosphate-buffered saline, burst release occurs. This is followed by the next phase in which a power-law relationship is observed between the cumulative amount of drug released and time.[71] The presence of dextran as a gating agent could also be the cause of the sustained DOX and DOX-A release. Thus, the presence of dextran appears to provide physical barriers to drug transport across the nanoparticles, while limiting diffusion and erosion processes.[72,73]

Next, we fitted the drug release data to the kinetic modeols to understand the kinetics of in vitro drug (DOX and DOX-A) release from the silica-based nanoparticle drug delivery systems developed. The kinetic model that fitted the release data with the highest R^2 value was selected as the best model. Based on this criterion, the release of DOX and DOX-A drugs from the silica-based nanoparticles followed the Korsmeyer–Peppas kinetics model[45,71–73] (Table S2). The initial 60% of drug release is usually best fit by this power law model.[43,74] This models yields n values in the range $0.21 < n < 0.71$. The release exponent, n, of the Korsmeyer–Peppas model was then used to assign the mechanism of drug release from the different

15524981, 0, Downloaded from https://onlinelibrary.wiley.com/doi/10.1002/jbm.b.35185 by Egyptian National Sci. Network (Enstinet), Wiley Online Library on [08/11/2022]. See the Terms and Conditions (https://onlinelibrary.wiley.com/terms-and-conditions) on Wiley Online Library for rules of use; OA articles are governed by the applicable Creative Commons License

silica-based drug formulations. Anomalous transport (non-Fickian diffusion) was the mechanism driving the release of DOX from MCM-41 and MCM-B nanoparticles, while the release of DOX from MCM-B-D nanoparticles was driven by anomalous transport (non-Fickian diffusion) at 37°C, quasi-Fickian diffusion at 41°C, and Fickian diffusion at 44°C. The release mechanism of the DOX-A drug from all the silica-based nanoparticles (MCM-41, MCM-B, and MCM-B-D) were predominantly driven by quasi-Fickian diffusion.

It is important to note that the release profile of MCM-B-D-DOX-A in Figure 7E appears different from its counterparts in Figure 7D,F. As noted above, the MCM-B-D-DOX-A release profile in Figure 7E fitted a Korsmeyer–Peppas kinetic model with a quasi-Fickian drug release mechanism (release exponent, $n = 0.28$ [Table S2]). This means that DOX-A was partially diffusing into the surrounding medium through the swollen dextran capping the nanoparticles, thereby slowing down the amount of drug released. Although the release profile appears linear throughout, it is nonlinear for the first 2 days of release. This was likely the result of the initial release of the DOX-A drugs trapped in the dextran as it swelled. By the second day and over time, the fully swollen dextran continuously trapped the drugs diffusing out of the pores of the underlying nanoparticles and subsequently released them into the surrounding medium via quasi-diffusion at a relatively constant rate until day 30, accounting for the relatively linear profile observed between days 2 and 30. In addition, although not within the scope of this work, it is most likely that if the drug release duration is extended beyond 30 days, the release profile will eventually plateau when the dextran is degrading or has degraded and the drugs can directly diffuse out from the nanoparticle pores into the surrounding medium.

The diffusion coefficients obtained for the conjugated drug (DOX-A) formulations were higher than those obtained for the unconjugated drug (DOX) formulations. The diffusion coefficient (D) was in the range of $1.84 \times 10^{-23} \le D \le 4.17 \times 10^{-23} m^2 s^{-1}$ for the unconjugated drug (DOX) and $1.21 \times 10^{-22} \le D \le 4.26 \times 10^{-22} m^2 s^{-1}$ for the conjugated drug (DOX-A). This shows that the conjugated drug diffuses faster into the medium than the unconjugated drug.

The COMSOL simulation shows the average flux of the drug through the multiple pores of the nanomaterial over a month (Figure 8) and the time-dependent transport of diluted species from the concentration boundary showing that a line plot can be expressed as a 1D homogenized model which is synonymous to the cumulative drug release profile. This shows that the assumption that the bare and the functionalized silica nanoparticle are having pores in different direction is a good assertion as the cumulative flux after 30 days converges to a plot shown in Figure 8 that is synonymous with the cumulative drug release in Figure 7.

The release of drugs (DOX and DOX-A) from the drug-loaded nanoparticle formulations were correlated with reductions in the viability of PC-3 PC cells, hence the cell growth inhibition, to investigate whether the sustained release of DOX and DOX-A was beneficial for killing and inhibiting PC cell growth. A decrease in cell growth is expected to cause a reduction in cell viability. Therefore, lower percentage alamar blue reduction values corresponded to greater cell growth inhibition. On that basis, it was evident from Figure 9 that the drugs (DOX and DOX-A) released from the drug-loaded nanoparticles exerted significant antiproliferative effects on the PC-3 cells to cause the observed lower cell viabilities than the drug-free nanoparticles. Whereas the drug-free nanoparticles lowered cell viability by a factor of about 1.5, the drug-loaded nanoparticles reduced cell viability ~10-fold compared to the drug-free nanoparticles and ~16-fold versus the untreated cells, suggesting that the drugs released from the nanoparticles were more responsible for killing the cancer cells than the nanoparticles themselves.

The slow release of DOX and DOX-A drugs observed from the MCM-B and the dextran-capped MCM-B nanoparticles (Figure 7) did not correspond to lower cell viabilities of the MCM-41 nanoparticles. This suggests that the slowdown in drug release from the MCM-B nanoparticles owing to their smaller pore sizes did not translate into greater cell growth inhibition in vitro. Therefore, longer in vitro cell viability studies beyond 96 h as well as in vivo studies are needed to explore the effects of the prolonged drug release.

However, the slow release of AMACR antibody-conjugated drugs (DOX-A) from the nanoparticles was generally the most potent in inhibiting PC-3 cell growth. We showed in this study through immunofluorescence staining[75] (Figure S2) that AMACR proteins were expressed on the surfaces of the PC-3 PC cells. Additionally, we present optical images (Figure S3) from the immunohistochemical (IHC) staining of prostate tumors and benign prostatic hyperplasia (BPH) tissues extracted from patients at the National Hospital Abuja (under ethical clearance from the National Hospital Abuja) that reveal the overexpression of AMACR proteins on prostate tumors and not on the BPH tissues. Therefore, the greater cell growth inhibition associated with the sustained release of the AMACR antibody-conjugated drugs (DOX-A) from the nanoparticles was attributed to the binding of the AMACR antibody attached to the DOX drug to the AMACR proteins on the PC-3 cancer cells. This had the tendency of increasing the uptake of the drugs (DOX) by the cells through receptor-mediated endocytosis, leading to increased cell death.

It is worth noting that, although lower doses of drugs (DOX and DOX-A) were released from the drug-loaded nanoparticle formulations, the released drugs inhibited the growth of the PC-3 PC cells at similar levels as the directly added/unloaded drugs (DOX and DOX-A). Furthermore, the sustained release of low doses of AMACR antibody-conjugated DOX (DOX-A) from the silica-based drug delivery systems inhibited the PC-3 cancer cell growth more than the higher dose unloaded drugs (DOX and DOX-A). This suggests that by loading DOX and DOX-A into silica-based nanoparticles, the slowed release of the drugs can inhibit the growth of PC cells in vitro at the same level or even better than adding the drugs (DOX and DOX-A) directly to the cells.

Before closing, it is interesting to note that the three bare nanoparticles; MCM-41, MCM-B, and MCM-B-D supported the growth of the PC-3 cells to some extent, as shown in Figure 9. This work demonstrates that DOX and AMACR antibody-conjugated DOX can be loaded into silica-based nanoparticles with varying pore sizes to slow down and prolong drug release over a 30-day period. It also shows

15524981, 0, Downloaded from https://onlinelibrary.wiley.com/doi/10.1002/jbm.b.35185 by Egyptian National Sci. Network (Enstinet), Wiley Online Library on [08/11/2022]. See the Terms and Conditions (https://onlinelibrary.wiley.com/terms-and-conditions) on Wiley Online Library for rules of use; OA articles are governed by the applicable Creative Commons License

that AMACR antibody-conjugated drug-loaded formulations were more effective in inhibiting the growth of the PC-3 PC cells because of the specificity that was enabled by the conjugation of the DOX drug with AMACR antibody. The drugs are released in lower doses from the nanoparticles than the drugs that are directly treated to cells but inhibit the growth of PC cells at similar levels or even better. This is beneficial for reducing the amount of highly toxic cancer drugs, such as DOX, in the patient and could potentially shrink/eliminate prostate tumors in vivo while reducing side effects7. Further work is needed to demonstrate these effects under in vivo conditions.

5 | CONCLUSIONS

This article presents the results of a combined experimental and theoretical/computational study of the targeted delivery of untargeted (DOX) and targeted (DOX-A) cancer drugs from silica nanoparticles to PC cells. Salient conclusions arising from the study are summarized below.

1. Silica nanoparticle structures can be engineered to have controlled pore sizes, volumes, and surface areas. The cumulative drug release from these structures also increases with increasing temperature, for temperatures between 37 and 44°C.
2. Drug release from the conjugated drug (DOX-A)-loaded nanoparticle formulations occurs predominantly by quasi-Fickian diffusion, while that of the unconjugated drug (DOX) formulation occurs predominantly by anomalous transport diffusion.
3. The specific targeting of the PC cells is enhanced by the conjugation of DOX to AMACR antibody and loading them into the silica nanoparticles. The sustained release of AMACR antibody-conjugated DOX enhances the specific targeting of PC cells for killing by the attached DOX, through the binding of the AMACR antibody moiety to the overexpressed AMACR proteins on the cells, thereby lowering PC cell viability.
4. Estimated drug release profiles similar to the experimental results through a silica nanoparticle drug formulation can be obtained through simulations following set diffusion principles and valid assumptions based on the TEM particle size. This has been validated by the convergence of the 30-day simulation plot and the 1D homogenized plot.

ACKNOWLEDGMENTS

This work was supported by the Pan African Materials Institute (PAMI) supported by the World Bank (WB) African Centres of Excellence (ACE) program at AUST (Grant No. PAMI P126974). Toyin Aina is also grateful to Professor M. Eswaramoorthy, faculty, staff and students in the Nanomaterials and Catalysis Laboratory at the Jawaharlal Nehru Centre for Advanced Scientific Research (JNCASR) in Bangalore, India.

CONFLICT OF INTEREST

The authors declare no potential conflict of interest.

DATA AVAILABILITY STATEMENT

The data that support the findings of this study are available from the corresponding author upon reasonable request.

REFERENCES

1. Sung H, Ferlay J, Siegel RL, et al. Global cancer statistics 2020: GLOBOCAN estimates of incidence and mortality worldwide for 36 cancers in 185 countries. *CA Cancer J Clin*. 2021;71(3):209-249. doi:10.3322/caac.21660
2. Nguyen-Nielsen M, Borre M. Diagnostic and therapeutic strategies for prostate cancer. *Semin Nucl Med*. 2016;46(6):484-490. doi:10.1053/J.SEMNUCLMED.2016.07.002
3. Bock N, Kryza T, Shokoohmand A, et al. In vitro engineering of a bone metastases model allows for study of the effects of antiandrogen therapies in advanced prostate cancer. *Sci Adv*. 2021;7(27):1-4. doi:10.1126/sciadv.abg2564
4. Pinto J, Athanassiou A, Fragouli D. Surface modification of polymeric foams for oil spills remediation. *J Environ Manage*. 2018;206:872-889. doi:10.1016/j.jenvman.2017.11.060
5. Lindner U, Lawrentschuk N, Weersink RA, et al. Focal laser ablation for prostate cancer followed by radical prostatectomy: validation of focal therapy and imaging accuracy. *Eur Urol*. 2010;57(6):1111-1114. doi:10.1016/J.EURURO.2010.03.008
6. Vallet-Regi M, Rámila A, Del Real RP, Pérez-Pariente J. A new property of MCM-41: drug delivery system. *Chem Mater*. 2001;13(2):308-311. doi:10.1021/cm0011559
7. Perera M, Krishnananthan N, Lindner U, Lawrentschuk N. An update on focal therapy for prostate cancer. *Nat Rev Urol*. 2016;13(11):641-653. doi:10.1038/nrurol.2016.177
8. Evans AJ. Treatment effects in prostate cancer. *Mod Pathol*. 2018;31(1):110-121. doi:10.1038/modpathol.2017.158
9. Cardwell CR, O'Sullivan JM, Jain S, Hicks BM, Devine PA, McMenamin ÚC. Hormone therapy use and the risk of acute kidney injury in patients with prostate cancer: a population-based cohort study. *Prostate Cancer Prostatic Dis*. 2021;24:1055-1062. doi:10.1038/s41391-021-00348-x
10. Barqawi AB, Rodrigues Pessoa R, Crawford ED, et al. Boosting immune response with GM-CSF optimizes primary cryotherapy outcomes in the treatment of prostate cancer: a prospective randomized clinical trial. *Prostate Cancer Prostatic Dis*. 2021;24:750-757. doi:10.1038/s41391-021-00321-8
11. Gravis G, Audenet F, Irani J, et al. Chemotherapy in hormone-sensitive metastatic prostate cancer: evidences and uncertainties from the literature. *Cancer Treat Rev*. 2017;55:211-217. doi:10.1016/j.ctrv.2016.09.008
12. Nichols JW, Bae YH. Odyssey of a cancer nanoparticle: from injection site to site of action. *Nano Today*. 2012;7(6):606-618. doi:10.1016/j.nantod.2012.10.010
13. Ashrafizadeh M, Deldar M, Paskeh A, et al. Targeting autophagy in prostate cancer: preclinical and clinical evidence for therapeutic response. *J Exp Clin Cancer Res*. 2021;41:105. doi:10.1186/s13046-022-02293-6
14. George R, Hehlgans S, Fleischmann M, Rödel C, Fokas E, Rödel F. Advances in nanotechnology-based platforms for survivin-targeted drug discovery. *Expert Opin Drug Discov*. 2022;17:733-754. doi:10.1080/17460441.2022.2077329
15. Khoobchandani M, Khan A, Katti KK, et al. Green nanotechnology of MGF-AuNPs for immunomodulatory intervention in prostate cancer therapy. *Sci Rep*. 2021;11(1):16797. doi:10.1038/S41598-021-96224-8
16. Upadhyay TK, Ali MI, Khan F, et al. Nanoparticles mediated target-specific drug delivery in prostate cancer: In-depth review. *Curr Med Chem*. 2021;29:4170. doi:10.2174/0929867329666211221112312

15524981, 0, Downloaded from https://onlinelibrary.wiley.com/doi/10.1002/jbm.b.35185 by Egyptian National Sci. Network (Enstinet), Wiley Online Library on [08/11/2022]. See the Terms and Conditions (https://onlinelibrary.wiley.com/terms-and-conditions) on Wiley Online Library for rules of use; OA articles are governed by the applicable Creative Commons License

17. Mladenović M, Morgan I, Ilić N, et al. Ph-responsive release of ruthenium metallotherapeutics from mesoporous silica-based nanocarriers. *Pharmaceutics*. 2021;13(4):460. doi:10.3390/pharmaceutics13040460
18. Day CM, Sweetman MJ, Song Y, Plush SE, Garg S. Functionalized mesoporous silica nanoparticles as delivery systems for doxorubicin: drug loading and release. *Appl Sci*. 2021;11(13):6121. doi:10.3390/app11136121
19. Zhang Y, Eltayeb O, Meng Y, et al. Tumor microenvironment responsive mesoporous silica nanoparticles for dual delivery of doxorubicin and chemodynamic therapy (CDT) agent. *New J Chem*. 2020;44(6):2578-2586. doi:10.1039/c9nj05427h
20. Silveira CP, Apolinário LM, Fávaro WJ, Paula AJ, Durán N. Doxorubicin-functionalized silica nanoparticles incorporated into a thermoreversible hydrogel and intraperitoneally administered result in high prostate antitumor activity and reduced cardiotoxicity of doxorubicin. *ACS Biomater Sci Eng*. 2016;2(7):1190-1199. doi:10.1021/ACSBIOMATERIALS.6B00241/SUPPL_FILE/AB6B00241_SI_001.PDF
21. Dau TAN, Le VMH, Pham TKH, et al. Surface functionalization of doxorubicin loaded MCM-41 mesoporous silica nanoparticles by 3-aminopropyltriethoxysilane for selective anticancer 9 effect on A549 and A549/DOX cells. *J Electron Mater*. 2021;50(5):2932-2939. doi:10.1007/s11664-021-08813-y
22. Jiang N, Zhu S, Chen J, Niu Y, Zhou L. A-methylacyl-CoA racemase (AMACR) and prostate-cancer risk: a meta-analysis of 4,385 participants. *PLoS One*. 2013;8(10):e74386. doi:10.1371/JOURNAL.PONE.0074386
23. Ping F, Chunyin B, Bin C, Na L, Jifeng W. Screening of differentially expressed genes and identification of AMACR as a prognostic marker in prostate cancer. *Andrologia*. 2021;53:15. doi:10.1111/and.14067
24. Erdogdu IH, Tuna B, Yorukoglu K, Montironi R. Biomarkers in urinary tract and male genital system carcinomas. *Biomarkers in Carcinoma of Unknown Primary*. Springer Nature; 2022:37. doi:10.1007/978-3-030-84432-5_9
25. Yamada H, Tsuzuki T, Maeda N, et al. Alpha methylacyl-CoA racemase (AMACR) in prostate adenocarcinomas from Japanese patients: is AMACR a "race"-dependent marker? *Prostate*. 2013;73(1):54-59. doi:10.1002/PROS.22539
26. Carnell AJ, Kirk R, Smith M, Mckenna S, Lian LY, Gibson R. Inhibition of human α-methylacyl CoA racemase (AMACR): a target for prostate cancer. *ChemMedChem*. 2013;8(10):1643-1647. doi:10.1002/CMDC.201300179
27. Sayari A. Catalysis by crystalline mesoporous molecular sieves. *Chem Mater*. 1996;8(8):1840-1852. doi:10.1021/cm950585+
28. Pavan Kumar BVVS, Salikolimi K, Eswaramoorthy M. Glucose-and pH-responsive charge-reversal surfaces. *Langmuir*. 2014;30(16):4540-4544. doi:10.1021/la500407r
29. Sun S-W, Lin Y-C, Weng Y-M, Chen M-J. Efficiency improvements on ninhydrin method for amino acid quantification. *J Food Compos Anal*. 2006;19:112-117. doi:10.1016/j.jfca.2005.04.006
30. Ippolito JE, Brandenburg MW, Ge X, et al. Extracellular pH modulates neuroendocrine prostate cancer cell metabolism and susceptibility to the mitochondrial inhibitor niclosamide. *PLoS One*. 2016;11(7):26. doi:10.1371/journal.pone.0159675
31. Aina T, Danyuo Y, Oparah J, et al. Release kinetics of fungicidal antimicrobials into packaged foods. *J Food Saf*. 2021;41:e12904. doi:10.1111/jfs.12904
32. Jusu SM, Obayemi JD, Salifu AA, et al. Plga-cs-peg microparticles for controlled drug delivery in the treatment of triple negative breast cancer cells. *Appl Sci*. 2021;11(15):7112. doi:10.3390/app11157112
33. Bruschi ML. *Strategies to Modify the Drug Release from Pharmaceutical Systems*; Woodhead Publishing 2015. Accessed June 4, 2022. http://www.sciencedirect.com/science/article/pii/B9780081000922000060.
34. Nurhan AD. Dash, Murthy. *Polish Pharm Soc*. 2010;67(3):217-223.
35. Gouda R, Baishya H, Qing Z. Application of mathematical models in drug release kinetics of carbidopa and levodopa ER tablets. *J Dev Drugs*. 2017;06(2):1-8. doi:10.4172/2329-6631.1000171
36. Akinboye ES, Rosen MD, Denmeade SR, Kwabi-Addo B, Bakare O. Sesign, synthesis, and evaluation of pH-dependent hyrolyzable emetine analogues as treatment for prostate cancer. *J Med Chem*. 2012;55:10. doi:10.1021/jm300426q
37. Akinboye ES, Rosen MD, Denmeade SR, Kwabi-Addo B, Bakare O. Design, synthesis, and evaluation of pH-dependent hydrolyzable emetine analogues as treatment for prostate cancer. 2021;10. doi:10.1021/jm300426q
38. Wójcik-Pastuszka D, Krzak J, Macikowski B, Berkowski R, Osiński B, Musiał W. Evaluation of the release kinetics of a pharmacologically active substance from model intra-articular implants replacing the cruciate ligaments of the knee. *Materials (Basel)*. 2019;12(8):1202. doi:10.3390/ma12081202
39. Korsmeyer RW, Gurny R, Doelker E, Buri P, Peppas NA. Mechanisms of solute release from porous hydrophilic polymers. *Int J Pharm*. 1983;15(1):25-35. doi:10.1016/0378-5173(83)90064-9
40. Lamprecht A, Yamamoto H, Takeuchi H, Kawashima Y. Microsphere design for the colonic delivery of 5-fluorouracil. *J Control Release*. 2003;90(3):313-322. doi:10.1016/S0168-3659(03)00195-0
41. Onwudiwe K, Obayemi J, Hu J, et al. Investigation of creep properties and the cytoskeletal structures of non-tumorigenic breast cells and triple-negative breast cancer cells. *J Biomed Mater Res Part A*. 2021;110:1004-1020. doi:10.1002/JBM.A.37348
42. Marsac PJ, Konno H, Taylor LS. A comparison of the physical stability of amorphous felodipine and nifedipine systems. *Pharm Res*. 2006;23(10):2306-2316. doi:10.1007/s11095-006-9047-9
43. Smith JM. Introduction to chemical engineering thermodynamics. *J Chem Educ*. 1950;27(10):584. doi:10.1021/ed027p584.3
44. Du X, Cheng Y, Liu Z, et al. CO_2 and CH_4 adsorption on different rank coals: a thermodynamics study of surface potential, Gibbs free energy change and entropy loss. *Fuel*. 2020;2021(283):118886. doi:10.1016/j.fuel.2020.118886
45. Obayemi JD, Jusu SM, Salifu AA, et al. Degradable porous drug-loaded polymer scaffolds for localized cancer drug delivery and breast cell/tissue growth. *Mater Sci Eng C*. 2020;112(March):110794. doi:10.1016/j.msec.2020.110794
46. Jusu SM, Obayemi JD, Salifu AA, et al. Drug-encapsulated blend of PLGA-PEG microspheres: in vitro and in vivo study of the effects of localized/targeted drug delivery on the treatment of triple-negative breast cancer. *Sci Rep*. 2020;10(1):14188. doi:10.1038/s41598-020-71129-0
47. De Souza RA, Chater RJ. Oxygen exchange and diffusion measurements: the importance of extracting the correct initial and boundary conditions. *Solid State Ion*. 2005;176(23–24):1915-1920. doi:10.1016/j.ssi.2005.05.010
48. Xu A, Zhao TS, Shi L, Xu JB. Lattice Boltzmann simulation of mass transfer coefficients for chemically reactive flows in porous media. *J Heat Transfer*. 2018;140(5):1-8. doi:10.1115/1.4038555
49. Sugimoto T, Hamamoto S, Nishimura T. Inhibited nanobubble transport in a saturated porous medium: effects of deposited colloidal particles. *J Contam Hydrol*. 2021;242:103854. doi:10.1016/j.jconhyd.2021.103854
50. Shafqat SS, Khan AA, Zafar MN, et al. Development of amino-functionalized silica nanoparticles for efficient and rapid removal of COD from pre-treated palm oil effluent. *J Mater Res Technol*. 2019;8(1):385-395. doi:10.1016/j.jmrt.2018.03.002
51. Hernández-Morales V, Nava R, Acosta-Silva YJ, Macías-Sánchez SA, Pérez-Bueno JJ, Pawelec B. Adsorption of lead (II) on SBA-15 mesoporous molecular sieve functionalized with -NH2 groups. *Micropor Mesopor Mater*. 2012;160:133-142. doi:10.1016/j.micromeso.2012.05.004

15524981, 0, Downloaded from https://onlinelibrary.wiley.com/doi/10.1002/jbm.b.35185 by Egyptian National Sci. Network (Enstinet), Wiley Online Library on [08/11/2022]. See the Terms and Conditions (https://onlinelibrary.wiley.com/terms-and-conditions) on Wiley Online Library for rules of use; OA articles are governed by the applicable Creative Commons License

52. Brody AL, Strupinsky ER, Kline LR. *Active Packaging for Food Application*. Vol 59. 1st ed. CRS Press; 2001.
53. Xue X, Gong H, Zheng H, Ye L. Boronic acid functionalized nanosilica for binding guest molecules. *ACS Appl Nano Mater*. 2021;4(3):2866-2875. doi:10.1021/ACSANM.1C00005/SUPPL_FILE/AN1C00005_SI_001.PDF
54. Quiles-Carrillo L, Montava-Jordà S, Boronat T, Sammon C, Balart R, Torres-Giner S. On the use of gallic acid as a potential natural antioxidant and ultraviolet light stabilizer in cast-extruded bio-based high-density polyethylene films. *Polymers (Basel)*. 2020;12(1):31. doi:10.3390/polym12010031
55. Panwar K, Jassal M, Agrawal AK. In situ synthesis of Ag-SiO_2 Janus particles with epoxy functionality for textile applications. *Particuology*. 2015;19:107-112. doi:10.1016/J.PARTIC.2014.06.007
56. Yang G, Lin Q, Wang C, et al. Synthesis and characterization of dextran-capped silver nanoparticles with enhanced antibacterial activity. *J Nanosci Nanotechnol*. 2012;12(5):3766-3774. doi:10.1166/jnn.2012.5865
57. Predoi G, Ciobanu CS, Iconaru SL, et al. Preparation and characterization of dextran coated iron oxide nanoparticles thin layers. *Polymers (Basel)*. 2021;13(14):2351. doi:10.3390/POLYM13142351
58. Denry I, Nédélec JM, Holloway JA. Tranexamic acid-loaded hemostatic nanoclay microsphere frameworks. *J Biomed Mater Res Part B Appl Biomater*. 2021;9:422-430. doi:10.1002/jbm.b.34918
59. Union I, Pure OF, Chemistry A. Recommendations for the characterization of porous solids (technical report). *Pure Appl Chem*. 1994;66(8):1739-1758. doi:10.1351/pac199466081739
60. Lim S, Ciuparu D, Pak C, et al. Synthesis and characterization of highly ordered Co-MCM-41 for production of aligned single walled carbon nanotubes (SWNT). *J Phys Chem B*. 2003;107(40):11048-11056. doi:10.1021/JP0304778
61. Albayati TM, Salih IK, Alazzawi HF. Synthesis and characterization of a modified surface of SBA-15 mesoporous silica for a chloramphenicol drug delivery system. *Heliyon*. 2019;5(10):e02539. doi:10.1016/j.heliyon.2019.e02539
62. Loy N, Preziosi L. *Mathematical Biology Kinetic Models with Non-Local Sensing Determining Cell Polarization and Speed According to Independent Cues*. Springer Berlin Heidelberg; 2019. doi:10.1007/s00285-019-01411-x
63. Czarnobaj K, Prokopowicz M, Greber K. Use of materials based on polymeric silica as bone-targeted drug delivery systems for metronidazole. *Int J Mol Sci*. 2019;20(6):1311. doi:10.3390/ijms20061311
64. Dell'isola GB, Cosentini E, Canale L, Ficco G, Dell'isola M. Noncontact body temperature measurement: uncertainty evaluation and screening decision rule to prevent the spread of covid-19. *Sensors (Switzerland)*. 2021;21(2):1-20. doi:10.3390/s21020346
65. Dash S, Murthy PN, Nath L, Chowdhury P. Kinetic modeling on drug release from controlled drug delivery systems. *Acta Pol Pharm Drug Res*. 2010;67(3):217-223.
66. Peppas NA, Sahlin JJ. A simple equation for the description of solute release. III. Coupling of diffusion and relaxation. *Int J Pharm*. 1989;57(2):169-172. doi:10.1016/0378-5173(89)90306-2
67. Danyuo Y, Dozie-Nwachukwu S, Obayemi JD, et al. Swelling of poly(N-isopropylacrylamide) P(NIPA)-based hydrogels with bacterial-synthesized prodigiosin for localized cancer drug delivery. *Mater Sci Eng C*. 2016;59:19-29. doi:10.1016/j.msec.2015.09.090
68. Lee H, Kim M, Kim SH, et al. Alpha-methylacyl-CoA racemase (AMACR), a potential new biomarker for glioblastoma. *Front Oncologia*. 2020;10:10. doi:10.3389/fonc.2020.550673
69. Bhattacharyya S, Wang H, Ducheyne P. Polymer-coated mesoporous silica nanoparticles for the controlled release of macromolecules. *Acta Biomater*. 2012;8(9):3429-3435. doi:10.1016/J.ACTBIO.2012.06.003
70. Kumar Jha M, Habibur Rahman M, Mofizur RM. Biphasic oral solid drug delivery system: a review. *IJPSR*. 2011;2(5):1108-1115.
71. Bouchoucha M, Côté MF, C-Gaudreault R, Fortin MA, Kleitz F. Size-controlled functionalized mesoporous silica nanoparticles for tunable drug release and enhanced anti-tumoral activity. *Chem Mater*. 2016;28(12):4243-4258. doi:10.1021/ACS.CHEMMATER.6B00877/SUPPL_FILE/CM6B00877_SI_001.PDF
72. Devi MG, Dutta S, Al Hinai AT, Feroz S. Studies on encapsulation of rifampicin and its release from chitosan-dextran sulfate capsules. *Korean J Chem Eng*. 2014;32(1):118-124. doi:10.1007/S11814-014-0161-9
73. Angelopoulou A, Efthimiadou EK, Kordas G. Dextran modified pH sensitive silica hydro-xerogels as promising drug delivery scaffolds. *Mater Lett*. 2012;74:50-53. doi:10.1016/J.MATLET.2012.01.054
74. Obayemi JD, Danyuo Y, Dozie-Nwachukwu S, et al. PLGA-based microparticles loaded with bacterial-synthesized prodigiosin for anticancer drug release: effects of particle size on drug release kinetics and cell viability. *Mater Sci Eng C Mater Biol Appl*. 2016;66:51-65. doi:10.1016/j.msec.2016.04.071
75. Obayemi JD, Salifu AA, Eluu SC, et al. LHRH-conjugated drugs as targeted therapeutic agents for the specific targeting and localized treatment of triple negative breast cancer. *Sci Rep*. 2020;10(1):8212. doi:10.1038/S41598-020-64979-1

SUPPORTING INFORMATION

Additional supporting information can be found online in the Supporting Information section at the end of this article.

How to cite this article: Aina T, Salifu AA, Kizhakkepura S, et al. Sustained release of alpha-methylacyl-CoA racemase (AMACR) antibody-conjugated and free doxorubicin from silica nanoparticles for prostate cancer cell growth inhibition. *J Biomed Mater Res*. 2022;1-19. doi:10.1002/jbm.b.35185

15524981, 0, Downloaded from https://onlinelibrary.wiley.com/doi/10.1002/jbm.b.35185 by Egyptian National Sci. Network (Enstinet), Wiley Online Library on [08/11/2022]. See the Terms and Conditions (https://onlinelibrary.wiley.com/terms-and-conditions) on Wiley Online Library for rules of use; OA articles are governed by the applicable Creative Commons License